ALL-OPTICAL DEMULTIPLEXING OF CLOSELY SPACED MULTIMEDIA RADIO SIGNALS USING SUB-PICOMETER FIBER BRAGG GRATING

by

Hatice Kosek
B.Eng., Ryerson University, Canada, 2004

A thesis
presented to Ryerson University
in partial fulfillment of the
requirement for the degree of
Master of Applied Science
in the Program of
Electrical and Computer Engineering.

Toronto, Ontario, Canada, 2006

Author's Declaration

I hereby declare that I am the sole author of this thesis.

I authorize Ryerson University to lend this thesis to other institutions or individuals for the purpose of scholarly research.

I further authorize Ryerson University to reproduce this thesis by photocopying or by other means, in total or in part, at the request of other institutions or individuals for the purpose of scholarly research.

Abstract

All-Optical Demultiplexing of Closely Spaced Multimedia Radio Signals Using Sub-Picometer Fiber Bragg Grating

© Hatice Kosek, 2006

Master of Applied Science
Electrical and Computer Engineering
Ryerson University

Subcarrier multiplexed (SCM) transmission of multimedia radio signals such as CATV (5-860 MHz), cellular wireless (900 MHz) and wireless LAN (2.4 GHz) over fiber is frequently used to deliver broadband services cost effectively. These multi-channel radio-over-fiber (ROF) links have interesting applications and can connect enhanced wireless hotspots that will support high speed wireless LAN services or low speed cellular services to different customers from the same antenna. The SCM signals need to be demultiplexed, preferably in the optical domain for many reasons. Prefiltering of SCM signals with fiber-based optical filters warrants the use of inexpensive photodetectors and increases network flexibility. However, realizing optical demultiplexing at sub-GHz level is challenging and thus necessitates optical filters with high selectivity and low insertion loss and distortion. We developed a novel sub-picometer all-optical bandpass filter by creating a resonance cavity using two closely matched fiber Bragg gratings (FBGs). This filter has a bandwidth of 120 MHz at -3 dB, 360 MHz at -10 dB and 1.5 GHz at -20 dB. Experimental results showed that the filter is capable of separating two radio frequency (RF) signals spaced as close as 50 MHz without significant distortion. When this demultiplexer was employed to optically separate 2.4 GHz and 900 MHz radio signals, it was found to be linear from -38 dBm to +6 dBm with $\sim$ 25.5 dB isolation. There was no significant increment in the BER of the underlying multimedia data. Results verified that the fabricated narrow bandpass filter can be a potential candidate in demultiplexing of RF signals in networks based on subcarrier multiplexed schemes.

Acknowledgments

I would like to express my sincere acknowledgement to my supervisor Dr. X. N. Fernando for his continuous guidance, patience and financial support throughout this thesis. His suggestions and advice were invaluable. I admire the fact that whenever I found it difficult to move on, he always had a solution.

I would like to immensely thank Dr. X. Gu for fabricating the fiber Bragg grating filters employed in the experiments. His support did not just stop at providing the gratings, his expertise in fiber optics have helped me expand my knowledge about many fiber optic devices and techniques. I was very fortunate to work with both Dr. Fernando and Dr. Gu, who had always encouraged and motivated me during my study. This thesis would not have been possible without their guidance. My thanks also go to Yifeng He for his willingness to collaborate with me.

I gratefully thank my family, especially my father, mother and brother, for their endless support, love and encouragement in the course of my study.

I would like to thank the Ontario Graduate Scholarship source and School of Graduate Studies for providing Ryerson Graduate Scholarship. Last but not the least, I would like to thank the Department of Electrical and Computer Engineering for providing me with a unique setting in Fiber Optic Sensing and Communication Lab and WINCORE Lab to carry out my research.

Contents

1 Introduction 1
- 1.1 Literature Survey . . . 5
- 1.2 Major Contributions of the Thesis . . . 6
- 1.3 Outline of the Thesis . . . 7

2 Background and Analysis of ROF Link 8
- 2.1 Radio over Fiber Link . . . 8
  - 2.1.1 External Modulation . . . 8
  - 2.1.2 Power Loss in the ROF Link . . . 12
  - 2.1.3 Noise Sources in the ROF Link . . . 12
- 2.2 Fiber Bragg grating . . . 15
  - 2.2.1 FBG Characteristics . . . 18
- 2.3 Narrow Band Fiber Optic Filter . . . 19
  - 2.3.1 Transmittance of FP-FBG . . . 20
- 2.4 Mathematical Analysis of FTTC System with FBG . . . 22
  - 2.4.1 Generation of Subcarrier Multiplexed Signals . . . 22
- 2.5 Dispersion Issues . . . 30
  - 2.5.1 Grating Dispersion . . . 30
  - 2.5.2 Fiber Chromatic Dispersion . . . 31

3 FBG Fabrication and Experimental Results 34
- 3.1 Fabrication of the FP-Based FBG . . . 34
- 3.2 Features of the Filter . . . 37
  - 3.2.1 Comparison of the Fabricated Filter with a Planer FP . . . 40
- 3.3 Experimental Setup . . . 43
  - 3.3.1 Bit Error Rate (BER) Estimation . . . 46
- 3.4 Experimental Results . . . 48
  - 3.4.1 Linearity of the Filter . . . 48
  - 3.4.2 Selectivity of the Filter . . . 50
  - 3.4.3 Frequency Separation of the Filter . . . 51
  - 3.4.4 Distortion Due to the Filter . . . 52
  - 3.4.5 Beat Noise . . . 55

3.5 Carrier Suppression 57
3.6 Cellular Upper Sideband Suppression 58

4 Discussions and Future Work **63**
4.1 Discussions 63
4.1.1 Chromatic Dispersion Issues 63
4.1.2 Power Loss and Noise in the Experimental Setup 64
4.2 Conclusions 64
4.3 Future Work 65

List of Figures

1.1 Radio-over-fiber based wireless access system incorporating subcarrier multiplexed cellular and wireless local area network (WLAN) radio signals 2

2.1 A point-to-point externally modulated ROF link and the transfer characteristics of the Mach-Zehnder modulator 10
2.2 Grating structure in the fiber core. 16
2.3 Block diagram of a SCM MOF system 23
2.4 Magnitude spectrum of the optical field at the MZM output 26
2.5 Magnitude spectrum of the transmitted field at filter output and the spectrum of the detected current 28
2.6 Magnitude spectrum of the reflected field at port 3 and the spectrum of the current at the detector output 29
2.7 The effect of chromatic dispersion on the received RF power with the fiber length for RF signals at 900 MHz and 2.4 GHz. 33

3.1 The setup used in fabricating fiber Bragg grating using Phase Mask technique 35
3.2 The fiber Bragg grating based Fabry-Perot filter 38
3.3 Transmission spectrum of the designed narrow bandpass filter. The spectrum was measured with an OSA at 15 pm resolution 39
3.4 The block diagram of the setup used in sweeping the spectrum of the central resonant peak 40
3.5 The spectrum of resonant peak (solid line), obtained by scanning the sideband over a 2 GHz range at 4 MHz per step. The thin line was the calculated resonant spectrum from a planer FP resonator 41
3.6 The central resonant peak scanned with the polarization state in non-optimal position. Faded trace is the non-optimized SOP case and the bolded trace represents the optimized SOP 42
3.7 Experimental setup used for achieving demultiplexing of two subcarrier multiplexed microwave channels at 900 MHz and 2.4 GHz with the sub-picometer bandpass filter 44

3.8 Optical spectra obtained on the optical spectrum analyzer. (a) output of the MZM when the DC bias was tuned to non-linear region (b) output of the MZM when the DC bias is tuned to linear region (c) lower sideband of the cellular signal selected by the filter 45
3.9 The eye diagram displayed on the Communication Analyzer and the representation of the parameters involved in calculating the Q-factor 47
3.10 Carrier-to-leakage ratio (CLR) versus the input RF power of 900 MHz when the filter selected the 900 MHz signal and reflected the 2.4 GHz signal to circulator output port 49
3.11 Received RF power versus input RF power of 900 MHz signal measured at the WCA when the 900 MHz signal is selected by the filter while the WLAN signal is reflected 51
3.12 The degree of isolation that can be achieved by the filter 52
3.13 Leakage power in 2.4 GHz after demultiplexing versus the input RF power of 2.4 GHz at the filter output 53
3.14 BER performance of 900 MHz when the 2nd subcarrier is scanned from 450 MHz to 1.1 GHz. This figure shows the minimum frequency separation of about 50 MHz permitted by the filter between two subcarriers 54
3.15 BER of cellular signal (900 MHz) versus the received RF power with and without filter 55
3.16 a) represents the eye diagram of the 900 MHz (selected) signal obtained at the output of the bandpass filter (b) is the 2.4 GHz signal (reflected) obtained at the output of the circulator (port 3) 56
3.17 The BER performance of 2.4 GHz at port 3 with the power ratio of 2.4 GHz and 900 MHz 57
3.18 BER versus the received optical power of 900 MHz with and without filtering. 59
3.19 The transmission spectrum of a second Fabry-Perot based fiber Bragg grating 60
3.20 The central resonant peak of the filter shown with a larger scale 61

List of Symbols

Greek Symbols	Description
Λ	Fiber Bragg grating period
Λ_{mask}	Phase mask corrugation period
λ_{Bragg}	Grating wavelength
Δ_n	Change in the core refractive index
Υ	Electro-optic coefficient
φ_o	Initial phase constant of the optical waveguide
φ_m	Modulated phase constant of the optical waveguide
α	Fiber attenuation in dB/km
ρ	Grating parameter
Ω	Coupling coefficient between the forward- and backward-propagating modes
β	Propagation constant of the fundamental LP_{01} mode
$\Delta\beta$	Detuning wave parameter
σ_B	Bragg wave number
$\eta(V)$	Modal overlap factor
ω_o	Angular frequency of the input optical carrier
ω_1, ω_2	Angular frequency of the subcarriers
μ_i	Mean of bits ones/zeros
σ_i	Standard deviation of bits ones/zeros
ν	Poisson's ratio

English Symbols	Description
B	Bandwidth
c	Speed of light
d	Distance where external electrical voltage is applied across in MZM
D	Fiber dispersion parameter
E(t)	rms complex envelope of the optical field of MZM
$E_{MZM}(t)$	Optical field at the output of MZM
E_o	rms optical field at the modulator input
$E_R(t)$	Instantaneous transmitted optical field
$E_T(t)$	Instantaneous reflected optical field

f	RF frequency
I_D	Average (DC) photocurrent
$i_R(\omega)$	Received photocurrent
$\langle I_{RIN}^2 \rangle$	Mean square value of relative intensity noise
$i_T(\omega)$	Transmitted photocurrent
$J_n(m)$	Bessel function of the first kind of order n
k_B	Boltzmann's constant
k_o	Free-space wave number
L	Distance between two mirrors of Fabry-Perot
L_c	Connector loss
L_f	Fiber length
L_g	Grating length
L_s	Distance between two gratings
L_{sp}	Splicing loss
L_t	Electrode length
m	Optical modulation index
m_1, m_2	Normalized RF amplitudes of the subcarriers
N	Number of users in a MOF system
n_c	Number of connectors
n_{core}	Non-modified refractive index
n_{eff}	Mode refractive index
n_{sp}	Number of splices
$P(t)$	Instantaneous output optical power for direct modulation
p_{11}, p_{12}	Stain-optic tensor components
$\langle \Delta P^2(t) \rangle$	Mean square intensity fluctuation of laser diode output optical power
P_{conv}	Accumulative loss of E/O conversion and O/E conversion
p_e	Effective strain-optic constant
P_o	Mean optical power
$P_{opt,in}$	Laser output power
$P_{out_{op}}(t)$	Output instantaneous power of MZM
P_{RF}	Detected RF power at the photodetector

P_{RIN}	Relative intensity noise parameter
$P_{ROFloss}$	Power loss in the ROF link
$P_{ROFloss,dB}$	Power loss in the ROF link in dB
q	Electron charge
Q	Q-factor
$R(L_g, \lambda)$	Grating reflectivity
$\Re$	Photodetector responsivity in mA/mW
R_L	Load resistance
s(t)	Normalized modulating RF signal in direct modulation
s_o	Fiber zero dispersion slope
T	Absolute temperature in Kelvin
$T_{FP}(\lambda)$	Transmission of Fabry-Perot
V	Fiber mode field parameter
V_1, V_2	RF voltage of subcarriers
V_b	MZM DC bias current
$V_M(t)$	Applied electrical voltage to the MZM
V_π	MZM half-wave voltage
z	Distance along the fiber axis

List of Abbreviations

Abbreviation	Description
3G	Third-Generation
ASE	Amplified spontaneous emission
ASK	Amplitude shift keying
BER	Bit-error-rate
BERT	Bit-error-rate tester
BPSK	Binary phase shift keying
CATV	Cable television
CBS	Central base station
CLR	Carrier-to-leakage ratio
CRC	Canadian Comunications Research Centre
CSR	Carrier-to-sideband ratio
DC	Direct Current
E/O	Electrical-to-optical
EDFA	Erbium doped fiber amplifier
F	Finesse
FBG	Fiber Bragg grating
FDM	Frequency division multiplexing
Fi-Wi	Fiber wireless
FP	Fabry-Perot
FP-FBG	Fabry-Perot fiber Bragg grating
FSR	Free spectral range
FTTC	Fiber-to-the-curb
FTTH	Fiber-to-the-home
FWHM	Full-width at half-maximum
HDTV	High defitinition television
LSB	Lower-sideband
MOF	Multimedia-over-fiber
MZM	Mach-Zehnder modulator
NRZ	Non-return to zero
O/E	Optical-to-electrical

OSA	Optical spectrum analyzer
PC	Personal computer
RAP	Radio access point
RF	Radio frequency
RIN	Relative intensity noise
ROF	Radio-over-fiber
SCM	Subcarrier multiplexed
SMF	Single mode fiber
SNR	Signal-to-noise ratio
SOP	State-of-polarization
SSB	Single sideband modulation
USB	Upper-sideband
UV	Ultraviolet
WCA	Wireless communication analyzer
WDM	Wavelength division multiplexing
WLAN	Wireless Local Area Network

Chapter 1

Introduction

IN the path towards fourth-generation networks, current communication systems are challenged with the demand for high date rate multimedia services and ubiquitious communications. The need for the increased bandwidth will be apparent with the emergence of data-hungry applications including video conferencing and high definition television (HDTV). In response to this challenge, current and future broadband wireless systems are expected to deliver medias such as voice, data and video with high quality at the lowest cost possible. Radio-over-fiber (ROF) schemes in conjunction with subcarrier multiplexed (SCM) radio signals can deliver multimedia wireless services to subscribers over a single optical fiber and address the need for abundant bandwidth cost effectively. These type of links have proven to deliver high quality multimedia services. An evidence of this is Utopia in Utah, USA, which provides high speed internet access, telephony and television programming through a fiber optic cable at 30 Mb/s to its 3000 subscribers in 14 cities. It is reported that this flexible system can be easily upgraded to support a data rate of 1 Gb/s.

Another foreseen evolution in multimedia service provision is the integration of WLAN network with the 3G and beyond cellular networks to typically provide hotspot coverage. Hotspots are ideal for crowded areas such as supermarkets, subway stations and airport concourses. Current WLAN standards based on IEEE and HIPERLAN/2 can provide data rate up to 54 Mb/s. In the future; however, the data rate is anticipated to reach 155 Mb/s. To meet this, the third generation cellular network must be reshaped to push the

data rate to the expected level and allow internetworking with the WLAN technology. The use of subcarrier multiplexed fiber radio scheme in this scenario should ease this transition. For example, fastly emerging fiber-to-the-home (FTTH) and less expensive fiber-to-the-curb (FTTC) are attractive systems for wireless access.

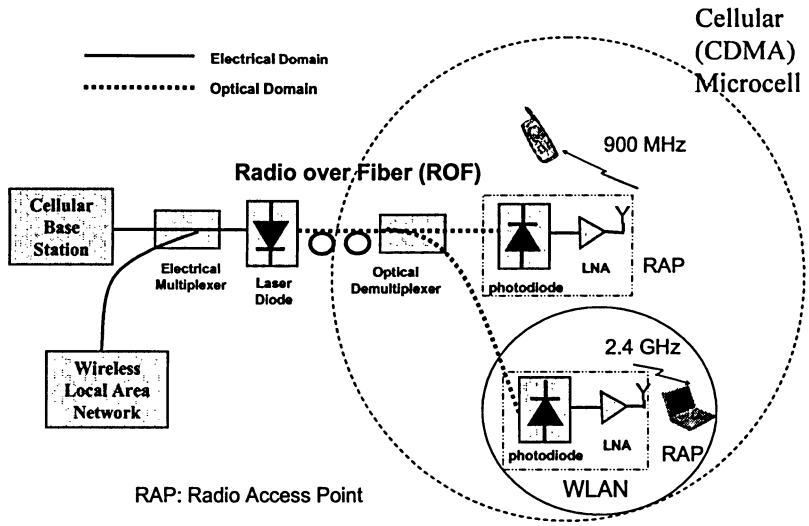

Figure 1.1: Radio-over-fiber based wireless access system incorporating subcarrier multiplexed cellular and wireless local area network (WLAN) radio signals

Figure 1.1 shows such a SCM fiber-to-the-curb wireless downlink, where cellular (900 MHz) and WLAN (2.4 GHz) radio signals are transmitted simultaneously from the central base stations (CBS) to remote wireless devices via radio-over-fiber link. FTTC delivers the voice and data oriented radio signals to the last mile wirelessly. The services can be of high quality because fiber is brought to the last mile and the air interface is short. The cellular signal originated from the cellular base station is electrically multiplexed with a WLAN radio signal at a microwave power combiner. The composite RF signal intensity modulates an optical carrier at the optical transmitter and then transmitted to the radio access point

(RAP) located at the user neighborhood. The RAP consists of simple devices and its main function is to convert the optical signals to electrical signals and vice versa. It serves as an extended antenna from the central base station. The RAPs with simple functions not only are inexpensive but their compact size can save estate cost.

Demultiplexing of such subcarrier multiplexed signals can be done either by the optical or the electrical domain bandpass filters. Figure 1.1 emphasizes on separating radio signals using an all-optical demultiplexer. The split signals can then be distributed to different RAPs, which provide voice or data services to wireless subscribers with mobile units such as cell phones, laptops or PCs. With such arrangement, a dual-mode mobile terminal with both cellular and WLAN interfaces can receive low-speed radio cellular service in a large coverage area while taking advantage of the high speed WLAN service within smaller fiber wireless (Fi-Wi) cells [1]. The advantage of an ROF based SCM architecture include reduction in cell size that improves spectral efficiency and increases frequency reuse. A single central base station can be connected to multiple RAPs via SCM ROF links, where flexible radio spectrum management is possible. The cost of the CBS deployment and operation is shared among many subscribers. Moreover, users can have network connectivity everywhere with high data rates and reasonable mobility. Substantial increase in the capacity is especially beneficial for dense urban areas, where hotspots can be used to respond to the needs of congested traffic. The more detailed advantages of this internetworking are presented by Doufexi et al. in [2].

Previous research has shown that isolation of radio signals in the optical domain can offer a promising performance [3]. The main advantages of all-optical demultiplexing include the following:

- All-optical demultiplexer adds flexibility to the optical link/network by allowing the tapping of any subcarrier at any point along the fiber length. This will enable better radio resource management in an optical fiber based wireless network.

- The optical receiver performance requirements are eased with optical demultiplexing. Since in this scenario, the receiver has to detect only a single RF channel, the photode-

tector and the following electrical devices could be of low bandwidth matched to only that RF band. Otherwise in conventional SCM systems, the receiver has to support all the subcarriers; therefore should be wideband. Wideband requirement increases the cost of deploying a receiver.

- In all-optical networks, unnecessary loss, noise and distortion due to optical-to-electrical (O/E) conversion and electrical-to-optical (E/O) conversion can be avoided.
- Cost-effective, low-loss and wavelength selective devices with high precision such as fiber Bragg gratings (FBG) can be employed. The continuous development of such devices allows the subcarrier multiplexed fiber systems to benefit from optical signal processing techniques.
- Dispersion induced products can be filtered out in the optical domain before their contribution as distortion mechanisms at the detector.

For an FBG to be an effective demultiplexer it must satisfy the following criteria:

- The filter should have a relatively low insertion loss.
- The filter must have a flat top reflection or transmission spectrum, which can be achieved by making the grating strong, either through high reflection spectrum or by imprinting a grating with higher length. However, the length can only be increased to a certain extend to still be able to athermally package the grating. If the spectrum has a constant amplitude over most of the channel bandwidth, the wavelength drift of the filter or the source can be overcome.
- The selectivity of the filter should be high to minimize the crosstalk, the amount of residual power *leaking* from an adjacent channel. This requires the filter to have a single peak with all the higher order peaks suppressed. This can be realized with apodization techniques, which increase the filter's ability to remove out of band channels.

1.1 Literature Survey

Optical filtering has long been investigated in digital multiple access systems; however, research has only been limited to frequency division multiplexing (FDM) or wavelength division multiplexing (WDM). As the following literature survey shows little effort has been put into demultiplexing of microwave SCM signals particularly at sub-GHz range due to the necessity for very narrow optical filters with appreciable performance.

First demonstration of optical prefiltering was done by Greenhalgh et al., who proposed to employ a Fabry-Perot etalon to filter a subcarrier prior to detection [4]. In the paper, a 780 nm semiconductor laser was intensity modulated with two subcarriers conveying Amplitude Shift Keying (ASK) modulated data at 10 Mb/s. Two Fabry-Perot etalons were implemented; one functioned as a tunable optical prefilter with instrumental linewidth of 150 MHz and the other was utilized to manage the wavelength stability of the laser by adopting a wavelength locking mechanism. Only timing jitter performance of the demultiplexed subcarrier was studied under the condition of setting one subcarrier at 1 GHz with the second subcarrier scanned from 1.1 GHz to 2.8 GHz. In this experiment, few limitations were experienced. Despite all the efforts of locking the laser wavelength, the prefilter etalon still managed to drift restricting demultiplexing to be performed within the span of an hour before the selected signal experienced fading. In addition, the impact of non-ideal spectral features of the prefilter etalon, which can contribute to signal distortion, was not evaluated in depth.

Capmany et al. suggested assembling optical demultiplexing in a system, where both WDM and SCM technologies were combined [5]. Isolating microwave signals in a WDM-SCM system with a Fabry-Perot filter is quite challenging due to the Fabry-Perot's periodical peaks, which can have an effect on the other existing RF channels. To overcome this issue, they reported a demultiplexer based on an FBG in conjunction with a Fabry-Perot. Digital pseudorandom Non-Return to Zero (NRZ) modulation was applied to two microwave signals at 2.44 GHz and 1.7 GHz at a data rate of 53 Mb/s. They realized a two-stage system, where the wavelength channel of interest was selected by an FBG first and then the microwave

channel residing in the SCM band was extracted using the Fabry-Perot prefilter. The filter's bandwidth was 170 MHz with the free spectral range of 5 GHz and the finesse of 205. The suitability of the applied technique was proved by judging the eye diagrams of the demultiplexed signals. The eye diagram of the selected channel showed crosstalk from the non-selected microwave channel attributed to the slope of the Fabry-Perot.

Many researchers have kept their focus on optical filtering at high microwave frequencies for several reasons. Few investigated single sideband modulation (SSB), extraction of a microwave sideband from the SCM signals, to combat chromatic dispersion. As the microwave frequency is increased, the demands on the filter characteristics are more relaxed. In contrast, demultiplexing of densely distributed microwave signals has stringent requirements since the filter should isolate the desired signal with no additional distortion.

1.2 Major Contributions of the Thesis

Extensive research has not been done in the area of optical demultiplexing of multimedia signals at low frequencies, which this thesis focusses on. The major contribution of this thesis is the experimental study of the fabricated novel Fabry-Perot based optical bandpass filter in all-optical demultiplexing of cellular (900 MHz) and WLAN (2.4 GHz) microwave signals [6], [7]. Mathematical analysis of an externally modulated MOF system was carried out to examine the performance of the optical field at various stages in the link. The experimental results were obtained when the filter was incorporated in a SCM FTTC downlink to isolate the cellular signal from WLAN signal. Series of experiments were performed to i) determine the selectivity of the filter ii) characterize the linearity of the filter iii) determine the minimum allowed frequency separation between two subcarriers iv) study the distortion effect of the filter on the reflected and the transmitted signals and v) investigate the beat noise at the reflecting port of the optical circulator and the carrier suppression.

1.3 Outline of the Thesis

The remainder of this thesis is organized in the following manner:

Chapter 2: Introduction This chapter gives an overview of the fiber optical link, where the external modulation of a laser is discussed in depth. The optical loss and noise sources in these type of links are identified and explained briefly. Following, the fundamentals of fiber Bragg grating (FBG) technology is introduced. The mathematical analysis of a MOF link employing an ideal FBG bandpass filter is presented. Finally, the last section focusses on the dispersion effects induced by the optical fiber and the Bragg grating.

Chapter 3: FBG Fabrication and Experimental Results The design and fabrication of a novel narrowband Fabry Perot FBG is described in detail. Implementation of the optical filtering technique that separates two microwave signals is detailed. The experimental results showing various aspects of the filter and their significance are presented. Filter linearity and distortion, system dynamic range, frequency separation, carrier suppression are few of the areas discussed. Lastly, the relation between the strain and FBG length and its application in the experiment is explained.

Chapter 4: Discussions and Future Work The 'chromatic dispersion as well as power loss and noise experienced in the SCM system are given. The remainder of this chapter summarizes the analytical and experimental results confirming the high performance of the filter deployed in this thesis. Suggestions for possible future implementations to improve the results are detailed.

Chapter 2

Background and Analysis of ROF Link

2.1 Radio over Fiber Link

Radio-over-fiber (ROF) schemes employing subcarrier multiplexing (SCM) promise good performance in internetworking of WLAN and cellular radio signals. ROF link is an interface between the central base station and the base stations. Such a link consists of a laser transmitter or a laser transmitter with an external modulator, which superimposes the microwave signal onto an optical carrier to allow transmission over fiber. The types of fiber may be multi mode or single mode and generally the latter is preferred due to its low loss and low dispersion. At the last mile of FTTC technology, an optical receiver consisting of a photodetector converts the optical signal back to the corresponding microwave signal. There are several notable advantages of fiber optics. Fiber is an excellent low-loss transmission medium allowing the distribution of RF signals over long distances in a broad bandwidth (several THz). Other benefits include flexibility, light weight and resistance to electro-magnetic interference (EMI), which generally contributes to noise during signal transmission.

2.1.1 External Modulation

The optical modulation of RF signals are often done using the two widely accepted modulation techniques classified as direct modulation and external modulation. In the direct modulation scheme, the RF signal directly modulates the bias current of the optical source

laser. External modulation on the other hand uses an intensity modulation device such as Mach-Zehnder (Y-branch interferometer) modulator following the laser. This modulator switches the laser light on and off without having an influence on the operation of the laser. Figure 2.1 shows the schematic representation of a point-to-point externally modulated radio-over-fiber optical link. Direct modulation of laser transmitter is simple and cost-effective to implement, but it has several constraints depending on the operating wavelength. Modulation bandwidth of the laser, which is typically 10 GHz at maximum, is a limiting phenomenon in applying direct modulation. There are also reports on lasers handling up to 40 GHz or even higher but these diodes are rather costly or commercially not available [8]. Clipping and frequency chirp are few of the inherent issues associated with this type of modulation. Alternatively, external modulation, which offers wide bandwidth, can be used to overcome the limitations imposed by direct modulation. Mach-Zehnder modulator is a highly developed and a widely used device and can support radio frequencies reaching over 110 GHz [9], a level that is impossible with direct modulation.

The operation of Mach-Zehnder modulator relies on the electro-optic effect, the basis in forming an intensity modulator. The optical signal emerging from the laser is divided into two beams, which initially have zero phase difference. The externally applied electric field on the electrodes imposes a small change in the refractive index of the electro-optic material (typically lithiumniobate $LiNbO_3$) in the modulator. Consequently, the optical field in that arm is phase shifted while the beam in the lower branch retains its original state. When an electric field E is applied across the two electrodes, the transversing light experiences phase shift given by

$$\varphi_m(t) = n(E)k_o L_t = \varphi_o - \frac{\pi V_M(t)}{L_t V_\pi} \tag{2.1}$$

where, $n(E)$ reflects the refractive index of the medium as a function of the applied electric field, $k_o = 2\pi/\lambda_o$ is the free-space wave number and φ_o is the initial phase constant of the optical waveguide. L_t is the electrode length and $V_M(t)$ denotes the time varying voltage applied to the modulator. V_π is the half-wave voltage needed to achieve a differential phase

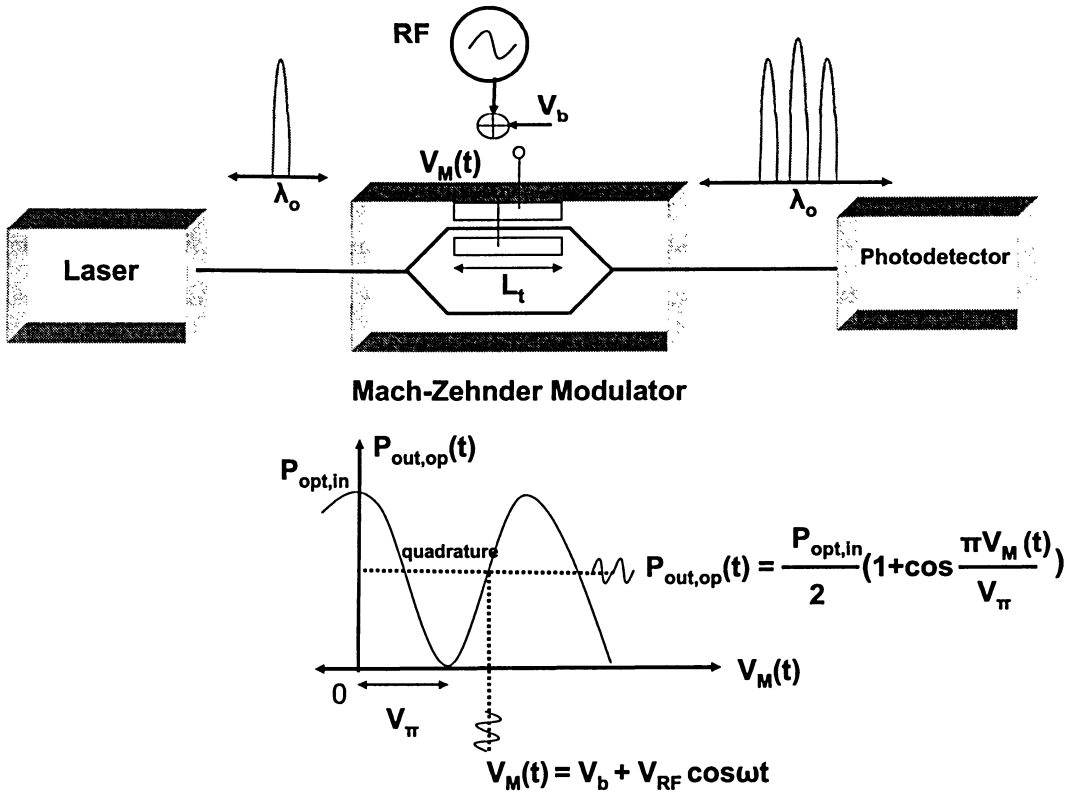

Figure 2.1: A point-to-point externally modulated ROF link and the transfer characteristics of the Mach-Zehnder modulator

shift of π between the two beams. At this voltage, the modulator's transmission is zero. V_π is expressed as

$$V_\pi = \frac{d\lambda_o}{L_t \Upsilon n^3} \tag{2.2}$$

where, Υ is the electro-optic coefficient and d is the distance where $V_M(t)$ is applied across. The two optical fields at the output are combined resulting in an intensity modulated optical signal.

The performance of the modulator is determined by several factors: applied voltage, impedance, optical loss, maximum input power the modulator can handle, bandwidth, linearity and sensitivity to temperature and polarization. Polarization dependent modulator, for instance, requires polarization controller to be included following the laser. The laser, which is typically linearly polarized, must match the state of the modulator to maximize the output optical power.

Al-Raweshidy and Komaki described a model, where they derived the relation between the applied voltage constituting of DC and RF voltages and the Mach-Zehnder modulator output [10]. The rms complex envelope of the optical field strength at the modulator output is

$$E(t) = \frac{E_{in}e^{j\phi}}{\sqrt{2}}(e^{-j\varphi_o L_t} + e^{-j\varphi_m(t)L_t}) \tag{2.3}$$

where E_{in} is the rms optical field at the modulator input. In the case of assuming the length of the electrodes to be much smaller than the modulating signal wavelength, the optical power can be written as

$$P_{out,op}(t) = |E|^2(t) = \frac{E_o^2}{2}[1 + cos[(\varphi_o - \varphi_m(t))L_t]] \tag{2.4}$$

With the assumption that $\varphi_m(t) = \varphi_o - (\pi V_M)/(LtV_\pi)$, the instantaneous power at the output of the modulator becomes

$$P_{out,op}(t) = \frac{P_{opt,in}}{2}[1 + cos\frac{\pi V_M(t)}{V_\pi}] \tag{2.5}$$

where $P_{opt,in}$ refers to the power available at the output of the laser.

As seen clearly from the transfer function of the modulator in Figure 2.1, a drawback associated with external modulation is the sinusoidal behavior exhibited by Mach-Zehnder modulator. The non-linear nature of the modulator limits its linear region to small range requiring biasing to be done at a half power (-3 dB) point. It is also known as the quadrature point representing the most linear region of operation.

2.1.2 Power Loss in the ROF Link

In the radio-over-fiber link, loss due to electrical-to-optical (E/O) conversion, connectors, fiber attenuation, optical-to-electrical (O/E) conversion and impedance mismatching between the 50 Ohms RF system are generally of concern. The overall power loss in the ROF link can be given by

$$P_{ROFloss,dB} = P_{conv} + 2(n_c L_c + \alpha L_f + n_{sp} L_{sp}) \tag{2.6}$$

$$P_{ROFloss} = 10^{(P_{ROFloss,dB}/10)} \tag{2.7}$$

P_{conv} is the accumulative loss of E/O conversion using the Mach-Zehnder modulator and O/E conversion at the receiving end. The second term reflects the loss experienced in the connectors. The number of connectors used in the link is n_c, L_c is the connector loss (typically 0.2 dB/connector). Third term is the fiber loss, α is the fiber attenuation (in dB/km) acquired within the fiber length of L_f. Attenuation in the fiber is wavelength dependent. For example, at 1550 nm, signal attenuation is only 0.2 dB/km. Nevertheless, fiber is still an excellent transmission medium compared to other existing channels such as coaxial cable. The last term in the above equation accounts for the loss due to splicing, permanent connection of two fibers. L_{sp} is splicing loss and n_{sp} is the number of splices. Splicing is generally required for longer links since fiber comes in spools of 1 to 5 km. Also, splicing can be used to avoid the larger loss incurred by overly used fiber connectors or pigtails. Typical splice loss with fusion splicing (in which fiber is aligned and fused to combine the two ends) is less than 0.03 dB.

2.1.3 Noise Sources in the ROF Link

Due to the electronic devices used in the detectors and the conversion process of photons to electrons, various noise sources such as shot(quantum) noise, thermal noise and dark current noise exist in the ROF link. In addition, laser also contributes a noise mechanism namely relative intensity noise (RIN) into the system.

Relative Intensity Noise

The intensity of laser output light is not stable. The fluctuations in the output signal are caused by the random spontaneous emission and temperature variations. There are also contributions by the noise from Brillouin scattering and intensity noise (interferometric noise) induced by multiple optical reflections back into the laser's active region. However, the optical reflections can simply be eliminated by inserting an optical isolator after the laser. All these noise sources are collectively referred to as relative intensity noise (RIN), which is solely dependent on the type of laser and the optical power.

The expression for the mean-square value for the RIN noise current is given by the following [11]

$$\langle I_{RIN}^2 \rangle = P_{RIN} \Re^2 P_o^2 B \tag{2.8}$$

where, P_{RIN} is the relative intensity noise parameter typically given in dB per unit bandwidth (dB/Hz). B is the bandwidth of the modulated signal, $\Re$ is the detector responsivity in mA/mW and P_o is the *mean* optical power. The parameter P_{RIN} is generally assumed to be constant for a given laser diode and ranges from -135 to -155 dB/Hz depending on the laser type. The RIN parameter is described as the ratio between the mean-square intensity fluctuation of the laser diode output optical power $\langle \Delta P^2(t) \rangle$ to the square of the mean optical power (P_o)

$$P_{RIN} = \frac{\langle \Delta P^2(t) \rangle}{P_o^2} \tag{2.9}$$

We can rewrite (2.8) by substituting P_{RIN} with the expression given in (2.9) and get

$$\langle I_{RIN}^2 \rangle = \langle \Delta P^2(t) \rangle \Re^2 B \tag{2.10}$$

The conventionally accepted intrinsic RIN expression (2.8) in directly modulated links only holds under small signal modulation single channel cases, where optical modulation index $m < 0.3$. However under large modulation conditions, RIN needs closer attention since

it is observed to also vary with m in subcarrier multiplexed multimedia over fiber (MOF) links. Traditionally, m used to be small; however, with the advent of optical signal processing techniques m can be very high. It was validated both analytically and experimentally by Fernando and Kosek in [12] that as the modulation index is increased, the relation of RIN power with m cannot be ignored. An improved expression for the RIN was derived with the assumption that the instantaneous optical power output $P(t)$ from the laser with the input electrical signal $s(t)$ is

$$P(t) = [1 + ms(t)][P_o + \Delta P(t)] \tag{2.11}$$

Then, the output photocurrent was passed through an ideal bandpass filter. The more accurate expression for RIN at the filter output is

$$\langle I_{RIN}^2 \rangle = P_{RIN} \Re^2 P_o^2 B[1 + \sum_{i=1}^{N} m_i^2 \left\langle s_i^2(t) \right\rangle] \tag{2.12}$$

where m_i is the i^{th} modulation depth of the signal $s_i(t)$, the normalized modulating RF signal in a MOF system with N users.

Shot noise

The optical signal is detected at the receiver in terms of photons. These photons arrive at the detector in a random manner causing a noise mechanism known as shot or quantum noise. The mean square shot noise current for a PIN diode is [13]

$$\langle I_s^2 \rangle = 2qI_D B = 2q\Re P_o B \tag{2.13}$$

where, q is the electron charge, $I_D = \Re P_o$ is the average (DC) photocurrent and B is the bandwidth of interest. P_o is the mean optical power incident on the photodiode and $\Re$ is the photodiode responsivity. Note that the shot noise is dependent on the DC current; therefore, the optical carrier power should be at acceptable level to minimize the shot noise produced at the receiver.

Thermal Noise

Thermal noise, also known as Johnson noise, is dependent on the load resistance of the photodetector. Thermal noise increases with the temperature of the load amplifier and it is represented by the given expression

$$\langle I_t^2 \rangle = \frac{4k_B TB}{R_L} \tag{2.14}$$

where k_B is Boltzmann's constant, T is the absolute temperature in Kelvin and R_L is the load resistance. As seen in Equation 2.14, thermal noise is independent of the optical signal and only relies on the resistance of the photodetector and the preamplifier.

2.2 Fiber Bragg grating

Fiber Bragg grating (FBG) is a corrugated structure where refractive index of the fiber core is permanently modified. This is achieved by exposing the core to an intense radiation in the ultraviolet (UV) range. Fiber Bragg grating reflects light in a narrow bandwidth centered at Bragg grating wavelength, $\lambda_{Bragg} = 2\Lambda n_{eff}$, where Λ is the grating (interference pattern) period and n_{eff} is the effective refractive index. As shown in Figure 2.2, an incoming optical signal that satisfies the λ_{Bragg} is reflected whereas the non-matching wavelengths are transmitted. However, the grating wavelength may be subject to slight shift with the variations in the fiber conditions such as polarization, temperature and strain.

Since the invention of Bragg gratings by the reputed researchers Kenneth Hill et al. in 1978 at the Canadian Communications Research Centre (CRC) in Ottawa, Canada, rapid and continuous development in the FBG technology has been witnessed. This has led the FBGs to be actively investigated and employed in wide range of applications in fiber optic telecommunications and sensor systems. These commercially available devices have key applications in dispersion compensation, wavelength selection, routing and EDFA (Erbium Doped Fiber Amplifier) gain flattening. FBGs also earned their place to fulfill other purposes as optical sensors, fiber mode converters and polarization mode converters. FBGs are widely

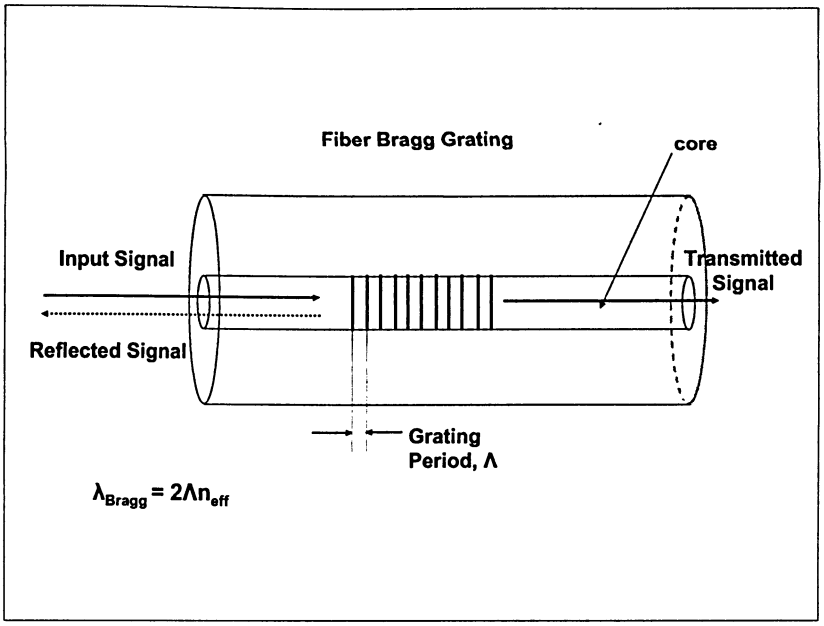

Figure 2.2: Grating structure in the fiber core.

accepted and a proven technology because they are inherently fiber compatible, passive, have low insertion loss, highly selective and furthermore can be packaged simply.

FBGs can be fabricated using several techniques, which include historically used holographic and internal techniques, point-by-point technique and the commonly used phase mask technique. Prior to fabrication of the grating in the core, the fiber goes through initial processing to increase the photosensitivity of the grating. Photosensitivity refers to the phenomenon of imposing a permanent change in the refractive index of the core in germanosilica fibers. High photosensitivity is achieved by using methods such as hydrogen loading or flame brushing [14]. In hydrogen loading, hydrogen molecules get diffused into the fiber core in a tube with pressure in the range of 100 to 300 atmosphere is applied in about 14 days. Flame brushing, as opposed to hydrogen loading, takes approximately 20 minutes to complete. A region in the fiber is brushed repeatedly with flame at an elevated temperature of about $1700°C$. The flame consists of hydrogen and partially oxygen. With this method,

the enhanced photosensitivity in the fiber is permanent, whereas the photosensitivity of a hydrogen loaded fiber decreases as the concentration of hydrogen is reduced.

KrF and ArF excimer lasers operating at 248 nm and 193 nm respectively are the commonly deployed radiation sources. These lasers generate optical pulses with duration in the order of 5-10 ns at a rate of 30-75 Hz. The radiated light directed through several stages depending on the adopted technique causes interference within the fiber core. The degree of change in the refractive index, which can vary between 10^{-5} to 10^{-3}, is dependent on the wavelength of the illuminating light, irradiation intensity and the core material as well as the processing technique used to prepare the fiber preceding to fabrication. The irradiated fiber has a perturbed core index, which holds a periodic structure comparable to a volume hologram or a crystal lattice behaving like a stop-band filter. The perturbation caused in the core along the fiber length of the grating has a sinusoidal profile given by

$$n(z) = n_{core} + \Delta n[1 + cos(\frac{2\pi z}{\Lambda})] \tag{2.15}$$

where, n_{core} is the non-modified refractive index and Δn is the refractive index change in the core. Λ represents the period of the interference pattern and z is the distance along the fiber axis. Note that the refractive index of the core is changed only in the areas where interference of the diffracted orders of the radiated light adds constructively. When the orders are out of phase, the core index retains its original refractive index value.

Following several minutes of radiation, annealing the grating in an oven for approximately 15 hours completes the transformation of a regular fiber into an optical passive device. Annealing the grating at a temperature of $150°C$, can shift the Bragg wavelength and compress the bandwidth and most importantly allows the grating to be used for as long as 25 years if properly done. In addition, any residual unreacted molecules in the fiber can be eliminated with exposure to high temperature.

2.2.1 FBG Characteristics

One of the main advantages of FBG technology is the flexibility it offers in controlling the spectral characteristics of the grating. The induced index change, grating length, apodization, period chirp, and whether the grating supports counter-propagating or co-propagating coupling of fiber modes at a desired wavelength can well be adjusted according to the application the grating is indented for. These variables allow the spectral and dispersive features of the grating to be tailored. FBGs are generally categorized as reflection gratings and transmission gratings. In transmission, co-propagation is supported while in reflection counter-progation takes place.

The full-width at half-maximum (FWHM) bandwidth also known as -3 dB bandwidth of the reflected or the transmitted signal is illustrated by

$$\Delta\lambda_{FWHM} \approx \lambda_{Bragg}\rho[(\frac{\Delta n}{2n_{core}})^2 + (\frac{\Lambda}{L_g})^2]^{1/2} \tag{2.16}$$

where the parameter ρ holds one for strong gratings with near 100% reflectivity and 0.5 for weak gratings. L_g denotes the length of the grating. The grating can further be classified as uniform and non-uniform. A uniform grating has a constant period along the grating length. The reflectivity for a uniform grating is expressed as [15]

$$R(L_g, \lambda) = \frac{\Omega^2 \sinh(SL_g)}{\Delta\beta^2 \sinh^2(SL_g) + S^2 \cosh^2(SL_g)} \tag{2.17}$$

here, Ω is the coupling coefficient between the forward- and backward-propagating modes. This parameter characterizes the strength of the grating. $\beta = 2\pi n_{eff}\sigma$ is the propagation constant of the fundamental LP_{01} mode. $\Delta\beta = 2\pi n_{eff}(\sigma - \sigma_B)$ is the phase-matching parameter that defines the detuning wave vector. σ is the wave number given by $\sigma = 1/\lambda$ and σ_B is the Bragg wave number. S is related to Ω and $\Delta\beta$ by $S = \sqrt{\Omega^2 - \Delta\beta^2}$. For sinusoidal index modulation Ω is

$$\Omega = \frac{\pi \Delta_n \eta(V)}{\lambda} \tag{2.18}$$

where, $\eta(V) \approx 1 - 1/V^2$ is the modal overlap factor as a function of V, which is the mode field parameter of the fiber. $\eta(V)$ quantifies the fraction of power that propagates in the core. At the center of the grating, the wave vector detuning $\Delta\beta$ is null, thus the expression in (2.18) simplifies to

$$R(L_g, \lambda) = \tanh^2(\Omega L_g) \tag{2.19}$$

As indicated in equation (2.19), the reflectivity of the grating is strongly determined by the index of refraction change as well as the length of the grating.

2.3 Narrow Band Fiber Optic Filter

Since the introduction of gratings, FBG technology has experienced major development in fabrication methods and potential applications with the goal to extend the use of these excellent devices. One type of FBG that has evolved over the last few years is narrow band fiber optic filters. There are several areas that require ultra-selective narrow bandwidth filters. These include high resolution strescopy, fiber laser, dispersion compensation for use as tracking filters for wavelength differentiation in structural sensing and demultiplexing of densely spaced microwave signals. These advanced filters are particularly suitable devices for channel selection in multi-channel systems, which expect the filters to meet stringent demands. The spectral shape of the optical filter needs to be free of sidelobes and ripples. It is also necessary for the filter to have steep slope with close to ideal spectral response.

FBG-based narrow bandpass filters can be designed using two methods if the FBG length is limited between 15 mm to 30 mm for the convenience of packaging. One is to induce a π-phase in the middle of the FBG that will create a narrow pass band in the center of the FBG's stop band. The phase shift is introduced in the refractive index pattern of the grating. The drawback of this technique is high insertion loss in the pass band of the FBG [16]. This

was also confirmed in our Fiber Optic Communication and Sensing Laboratory at Ryerson University. We fabricated a filter with a -3 dB bandwidth of 0.5 pm and we attained an insertion loss of 8 dB. Thus, phase-shifted technique is ruled out in designing a filter that is suitable for demultiplexing since it yields a very high insertion loss.

The second method is the FBG-based Fabry-Perot (FP-FBG) filter. The principle of FP-FBGs can be explained by FPs. Fabry-Perot is constructed with two spatially separated reflectors such as thin film multi-layer, metallic mirrors or fiber Bragg gratings. The optical light bounded by the two reflecting media bounces back and forth forming a resonator, also known as a cavity. In fiber Bragg grating based FP filters, the reflecting media are FBGs. When two highly reflective FBGs of identical wavelength form an optical cavity, the multiple reflections between them will create multiple resonant peaks in the stop band of the single FBG. The bandwidth of the resonant peak is determined by the spacing of the resonant peak and the reflectivity of the FBGs. Since the high reflectivity FBGs between -20 to -40 dB can be easily fabricated, the bandwidth of the resonant peak of less than a picometer can be realized. By combining the high selectivity of Fabry-Perot with the bandpass nature of FBG, an ultra-selective filter with high transmittance can be attained.

2.3.1 Transmittance of FP-FBG

Formulating an expression for the transmission of a Fabry-Perot fiber Bragg grating is challenging since complex analysis is involved. In addition, it is required for the model to approximate the transmission response for realistic filters that have Bragg gratings at slightly different wavelengths and with tapered refractive index profiles. The transmittance of this type of filter with multiple resonance peaks can be modelled by using two available approaches; matrix method and the model based on boundary conditions [17]. These methods depend on coupled-mode theory, the foundation used in computing the filter characteristics. They both yield results consistent with the experimentally obtained transmission spectrum; however, matrix method can proximate the transmission of more realistic FP-FBGs.

In the matrix method, the periodically structured grating is sectioned into elementary

layers. Each layer is assumed to have a periodical refractive index variation. It is critical to select the number of layers carefully for an accurate numerical calculation. Also, the layer length must be chosen such that it is relatively longer than the grating period Λ. The two gratings including the gap, where the fiber is non-modified, are characterized with ray-transfer matrices. Then, an equivalent matrix representing a single optical component is formed.

The analysis that makes use of the boundary conditions looks at the electric fields at the input and output of each grating and between the two gratings. The transmittance of the FP-FBG with this approach is defined as following [17]:

$$T(L_g,\lambda) = \frac{1}{1+4\{\frac{\Omega^2 sinh^2(SL_g)[\Omega^2 cosh^2(SL_g)-\Delta\beta^2]}{(\Omega^2-\Delta\beta^2)^2}\}cos^2[\Delta\beta L_g - \beta(L_s+L_g)-(\phi'/2)}} \tag{2.20}$$

where L_s is the separation between the two FBGs and ϕ' is derived from the given expression

$$tan\phi' = \frac{2\Delta\beta S sinh(SL_g)cosh(SL_g)}{S^2 cosh^2(SL_g) - \Delta\beta^2 sinh^2(SL_g)} \tag{2.21}$$

Equation (2.21) is true under the condition that the two Bragg gratings have precisely the same Bragg wavelength. Also, the refractive-index profile is assumed to be perfectly sinusoidal along the grating length. The reflectivity of the FP-FBG can simply be calculated from the following relation

$$R(L_g,\lambda) = 1 - T(L_g,\lambda) \tag{2.22}$$

In addition to the mentioned techniques, the spectrum of the FP-FBG can be compared to the one obtained by using the classical Fabry Perot equation.

2.4 Mathematical Analysis of FTTC System with FBG

2.4.1 Generation of Subcarrier Multiplexed Signals

In subcarrier multiplexed systems, each information-bearing baseband signal is mixed with a local oscillator at a different frequency, referred to as a subcarrier. The modulated carriers are subsequently summed via microwave power combiner and the combined signal modulates the laser carrier. Subcarrier multiplexed fiber links provide efficient utilization of the bandwidth while enabling multi-channels to be transferred to desired destinations. Typical application of subcarrier multiplexing is seen in Cable TV channel distribution.

In the microwave fiber-optical link, both the modulator and the photodetector are responsible for generating spectral components other than the sidebands of the SCM signals. This is evident in carrying out analysis when two subcarriers are simultaneously propagated. Figure 2.3 shows the block diagram of the system considered for the analysis. More specifically, the optical field at the output of the Mach-Zehnder modulator modulated on one arm is expressed as [10]

$$E_{MZM}(t) = E_o e^{j\omega_o t}(1 + e^{j\frac{\pi V_M(t)}{V_\pi}}) \tag{2.23}$$

where E_o and ω_o are respectively the optical field amplitude and angular frequency of the input optical carrier. $V_M(t)$ denotes the time varying voltage applied to the modulator and is described as follows in the case of two subcarriers,

$$V_M(t) = V_b + V_1 cos\omega_1 t + V_2 cos\omega_2 t \tag{2.24}$$

here ω_1 and ω_2 stand for the angular frequencies of the subcarriers and V_1 and V_2 are their respective RF peak voltages. V_b is the applied DC bias voltage. Hence, the overall output field when subcarrier multiplexed RF signals are applied to the external modulator can be written as

$$E_{MZM}(t) = E_o e^{j\omega_o t}(1 + e^{j\frac{\pi}{V_\pi}(V_b + V_1 cos\omega_1 t + V_2 cos\omega_2 t)}) \tag{2.25}$$

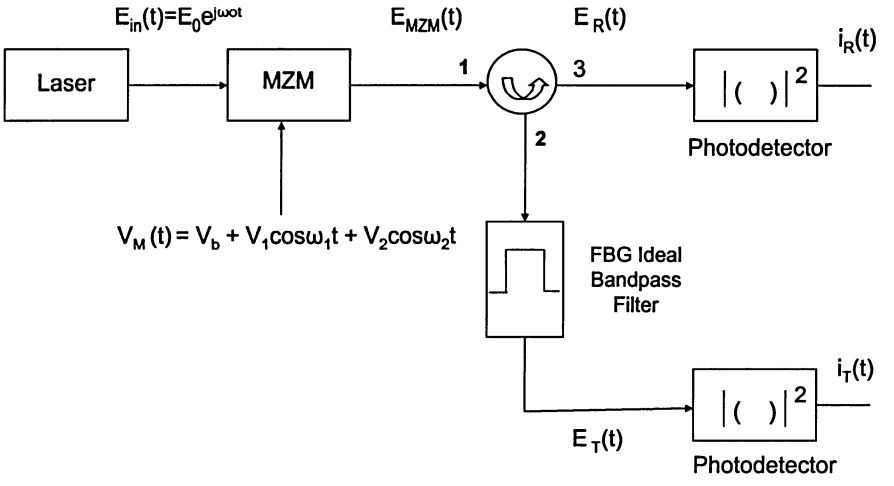

Figure 2.3: Block diagram of a SCM MOF system

Let us assume that $\phi = \pi V_b/V_\pi$, $m_1 = \pi V_1/V_\pi$ and $m_2 = \pi V_2/V_\pi$. m_1 and m_2 are the normalized RF amplitude of the first and the second subcarrier. When the condition of $V_b = V_\pi/2$ is satisfied, the MZM follows the quasilinear regime. Also, the amplitude of V_1 and V_2 need to be small in order to have a linear relationship between the input electrical signal and output optical signal. Under this operation, $\phi = \pi/2$, therefore (2.25) can be rewritten as

$$E_{MZM}(t) = E_o e^{j\omega_o t}(1 + je^{j(m_1 cos\omega_1 t + m_2 cos\omega_2 t)}) \tag{2.26}$$

Bessel function identity given in (2.27) can be used to expand the exponential functions for each RF signal.

$$e^{j(mcosx)} = \sum_{n=-\infty}^{\infty} j^n J_n(m) e^{jnx} \tag{2.27}$$

$J_n(m)$ is the Bessel function of the first kind of order n. Assume that

$$x(t) = e^{j(m_1 cos\omega_1 t + m_2 cos\omega_2 t)} \tag{2.28}$$

$$x(t) = \Big[\sum_{n=-1}^{1} j^n J_n(m_1) e^{jn\omega_1 t}\Big]\Big[\sum_{n=-1}^{1} j^n J_n(m_2) e^{jn\omega_2 t}\Big] \tag{2.29}$$

n was considered only from -1 to 1 since other orders are significantly lower under the narrowband modulation case. Therefore, it is reasonable to ignore Bessel function coefficients with orders higher than J_1.

Carrying out the expansion for $x(t)$ and using the property of the Bessel function of the 1^{st} kind, $J_{-n}(m) = (-1)^n J_n(m)$, we get

$$\begin{aligned} jx(t) = {} & jJ_0(m_1)J_0(m_2) - J_0(m_2)J_1(m_1)[e^{j\omega_1 t} + e^{-j\omega_1 t}] - J_0(m_1)J_1(m_2)[e^{j\omega_2 t} + e^{-j\omega_2 t}] \\ & - jJ_1(m_1)J_1(m_2)[e^{j(\omega_1+\omega_2)t} + e^{-j(\omega_1+\omega_2)t}] \\ & - jJ_1(m_1)J_1(m_2)[e^{j(\omega_1-\omega_2)t} + e^{-j(\omega_1-\omega_2)t}] \end{aligned} \tag{2.30}$$

Considering everything with respect to optical carrier frequency ω_o [1], the output optical field in equation (2.26) becomes,

$$\begin{aligned} E_{MZM}(t) = {} & E_o[1 + jJ_0(m_1)J_0(m_2) - J_0(m_2)J_1(m_1)[e^{j\omega_1 t} + e^{-j\omega_1 t}] - J_0(m_1)J_1(m_2)[e^{j\omega_2 t} + e^{-j\omega_2 t}] \\ & - jJ_1(m_1)J_1(m_2)[e^{j(\omega_1+\omega_2)t} + e^{-j(\omega_1+\omega_2)t}] \\ & - jJ_1(m_1)J_1(m_2)[e^{j(\omega_1-\omega_2)t} + e^{-j(\omega_1-\omega_2)t}]] \end{aligned} \tag{2.31}$$

[1] This is same as assuming ω_o=0

Because the dispersion effects of the fiber and the FBG filter are not dealt here, the phase part of the components in the optical field equation (2.31) can be ignored. Taking the Fourier transform with the phases neglected gives

$$\begin{aligned} E_{MZM}(\omega) = 2\pi E_o[&\sqrt{(1+J_0^2(m_1)J_0^2(m_2))}\delta(\omega) - J_0(m_2)J_1(m_1)[\delta(\omega-\omega_1)+\delta(\omega+\omega_1)] \\ &- J_0(m_1)J_1(m_2)[\delta(\omega-\omega_2)+\delta(\omega+\omega_2)] \\ &- J_1(m_1)J_1(m_2)[\delta(\omega-\{\omega_1+\omega_2\})+\delta(\omega+\{\omega_1+\omega_2\})] \\ &- J_1(m_1)J_1(m_2)[\delta(\omega-\{\omega_1-\omega_2\})+\delta(\omega+\{\omega_1-\omega_2\})]] \end{aligned} \tag{2.32}$$

To be able to plot the magnitude spectrum of the output field, the Bessel coefficients must be determined. This can be done by using the following expression [18]:

$$J_n(m) = \sum_{k=0}^{\infty} \frac{(-1)^k m^{2k+n}}{2^{2k+n}k!(n+k)!} \tag{2.33}$$

Assume that the voltages of the two subcarriers applied to the MZM have equal weight, $V_1 = V_2$, therefore $m_1 = m_2 = m$. This is also the case in the experiments done in the following chapter. When the MZM operates in the linear region, the sidebands are weakly modulated; therefore, the modulation index is small. If the modulation strength m is high, the modulator generates significant high-order harmonics that can lead to crosstalk between the signals. In practical situations, m must be much smaller than 1 in order to ignore the terms other than $J_1(m)$. Although keeping the modulation index at low values means inefficient modulation, non-linearity must be avoided. If $m = 0.1$, we determine $J_0(0.1) \approx 1$ and $J_1(0.1) \approx 0.05$. Taking $f_1 = \omega_1/2\pi$ as 900 MHz and f_2 as 2.4 GHz, the magnitude spectrum obtained from expression (2.34) is shown in Figure 2.4.

$$
\begin{aligned}
E_{MZM}(\omega) = 2\pi E_o[\sqrt{(1+J_0^4(m))}\delta(\omega) &- J_0(m)J_1(m)[\delta(\omega-\omega_1)+\delta(\omega+\omega_1)] \\
&- J_0(m)J_1(m)[\delta(\omega-\omega_2)+\delta(\omega+\omega_2)] \\
&- J_1^2(m)[\delta(\omega-\{\omega_1+\omega_2\})+\delta(\omega+\{\omega_1+\omega_2\})] \\
&- J_1^2(m)[\delta(\omega-\{\omega_1-\omega_2\})+\delta(\omega+\{\omega_1-\omega_2\})]]
\end{aligned} \tag{2.34}
$$

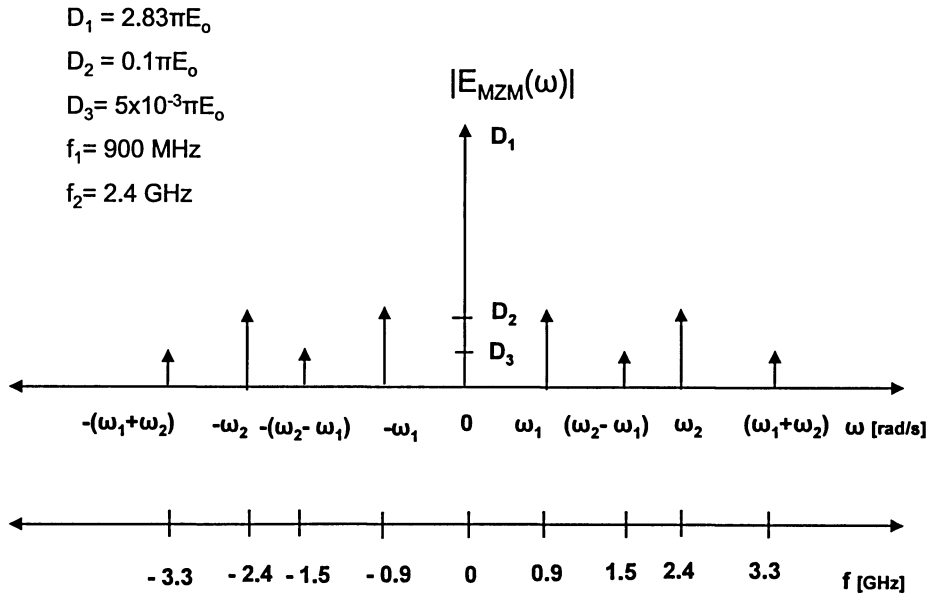

Figure 2.4: Magnitude spectrum of the optical field at the MZM output

Since the spectral components at $\pm(\omega_1 \pm \omega_2)$ are sufficiently lower than the components at $\pm\omega_1, \pm\omega_2$ and the DC, they can be neglected. The simplified MZM optical field is

$$
E_{MZM}(\omega) \approx 2\pi E_o[\sqrt{(1+J_0^4(m))}\delta(\omega) - J_0(m)J_1(m)[\delta(\omega-\omega_1)+\delta(\omega+\omega_1)]
$$

$$- J_0(m)J_1(m)[\delta(\omega - \omega_2) + \delta(\omega + \omega_2)]] \tag{2.35}$$

Note that the SCM signal has unmodulated optical carrier given by the expression $2\pi E_o\sqrt{(1 + J_0^4(m))}$ and the lower and upper sidebands (LSB and USB) corresponding to each subcarrier. Since each sideband carries identical information, extracting one sideband using narrow bandpass filter is sometimes adequate. The lower sideband of the subcarrier at ω_1 (900 MHz) together with partial carrier are selected by an FBG based ideal bandpass filter. The signal at the output of the filter is referred to as the transmitted optical field $E_T(\omega)$ expressed as

$$E_T(\omega) = 2\pi E_o[A\sqrt{(1 + J_0^4(m))}\delta(\omega) - J_0(m)J_1(m)\delta(\omega + \omega_1)] \tag{2.36}$$

The filtered out signal or the reflected signal at port 3 is given by

$$\begin{aligned} E_R(\omega) = 2\pi E_o[B\sqrt{(1 + J_0^4(m))}\delta(\omega) - J_0(m)J_1(m)\delta(\omega - \omega_1) \\ - J_0(m)J_1(m)[\delta(\omega - \omega_2) + \delta(\omega + \omega_2)] \end{aligned} \tag{2.37}$$

It is important to note that the optical carrier is distributed between the transmitted and the reflected signals. A and B are the fraction of the optical carrier transmitted and reflected respectively by the filter and A+B=1. The spectral response of the transmitted optical field is shown in Figure 2.5.

When the transmitted optical field is fed into a square law detector, the output photocurrent is

$$i_T(t) \propto \Re|E_T(t)|^2 \tag{2.38}$$

where $\Re$ implies the responsivity of the detector in (mA/mW) and typically takes the value of 0.9 mA/MW. Squaring in the time domain is same as performing convolution in the frequency domain.

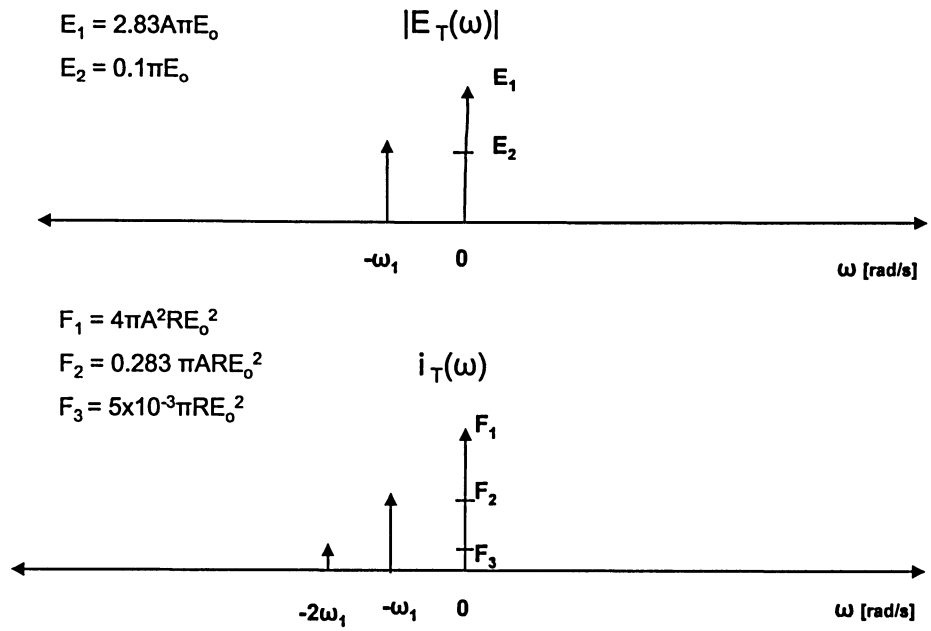

Figure 2.5: Magnitude spectrum of the transmitted field at filter output and the spectrum of the detected current

$$i_T(\omega) \propto \frac{\Re}{2\pi}|E_T(\omega) * E_T(\omega)| \tag{2.39}$$

Continuing with the derivation we get

$$i_T(\omega) \propto 2\pi\Re E_o^2[A^2(1+J_0^4(m))\delta(\omega) + 2A\sqrt{1+J_0^4(m)}J_0(m)J_1(m)\delta(\omega+\omega_1) + J_0^2(m)J_1^2(m)\delta(\omega+2\omega_1)] \tag{2.40}$$

As shown in Figure 2.5, the beating of the LSB of ω_1 with the carrier yields a spectral component at $-2\omega_1$. Similar to the transmitted field, the reflected field upon detection can be computed.

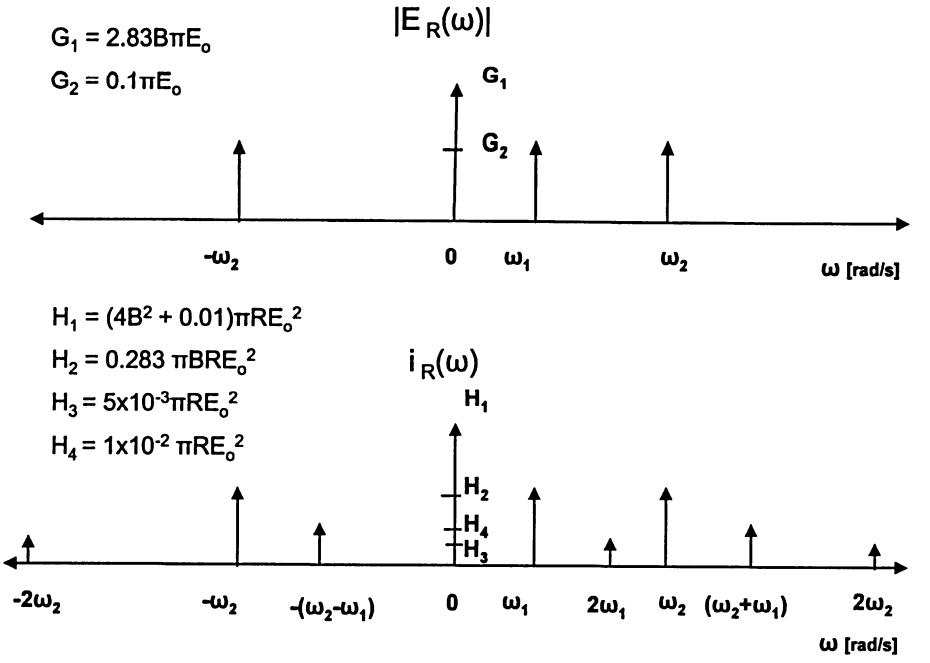

Figure 2.6: Magnitude spectrum of the reflected field at port 3 and the spectrum of the current at the detector output

$$
\begin{aligned}
i_R(\omega) \propto 2\pi \Re E_o^2 .
&[(B^2(1+J_0^4(m)) + 2J_0^2(m)J_1^2(m))\delta(\omega) \\
&+ 2B\sqrt{1+J_0^4(m)}J_0(m)J_1(m)\delta(\omega-\omega_1) \\
&+ 2B\sqrt{1+J_0^4(m)}J_0(m)J_1(m)\delta(\omega-\omega_2) \\
&+ 2B\sqrt{1+J_0^4(m)}J_0(m)J_1(m)\delta(\omega+\omega_2) \\
&+ J_0^2(m)J_1^2(m)\delta(\omega-2\omega_1) \\
&+ J_0^2(m)J_1^2(m)\delta(\omega-2\omega_2) \\
&+ J_0^2(m)J_1^2(m)\delta(\omega+2\omega_2)
\end{aligned}
$$

$$+ 2J_0^2(m)J_1^2(m)\delta(\omega - \{\omega_2 + \omega_1\})$$
$$+ 2J_0^2(m)J_1^2(m)\delta(\omega + \{\omega_2 - \omega_1\})] \quad (2.41)$$

The spectrum of the reflected photocurrent is depicted in Figure 2.6. From Figure 2.5, $-2\omega_1$ can always be easily filtered out. From Figure 2.6, ω_2 can be filtered out when ω_1, $2\omega_1$ and $(\omega_1+\omega_2)$ are considerably away from ω_2. We experimentally found that when $|\omega_1$-$\omega_2| \geq 50$ MHz and $\omega_1 = 900$ MHz, this was possible. In this case, $2\omega_1 = 1800$ MHz and $\omega_1+\omega_2 \geq 1850$ MHz when $\omega_2-\omega_1 \geq 50$ MHz, we did not have difficulty filtering ω_2. Actually, more stringent requirement is imposed by the FBG.

2.5 Dispersion Issues

2.5.1 Grating Dispersion

Fiber Bragg gratings perform exceptionally well as optical filters. However, generally dispersion due to grating is considered as a concern if the dispersion profile is not carefully optimized. The phase response of the grating dictates the dispersive properties of the filter. Previous investigations have found the grating dispersion to be a serious issue in WDM systems where signals at high rates are transmitted densely over long distances. This effect holds when the FBG is used both in reflection and transmission mode [19]. Note that in this case *the optical carrier is modulated at the transmission bit rate directly.* Hence, dispersive effect on the optical carrier will severely degrade the BER performance.

However, in radio over fiber systems, there are two levels of modulation (and frequency translation). The baseband information (few Mbps) is modulated on the radio signal (few GHz) and the radio signal in turn modulates the optical carrier (few THz). The FBG dispersion effects the THz optical signal, which in turn effects GHz RF signal, which as a result effects the baseband information. Therefore, the impact on baseband symbols is very little. This phenomena is also investigated in mm-wave fiber radio systems [20], [21]. It was also found by experiment that the effect of FBG dispersion or distortion on the baseband

BER is insignificant (Figure 3.15).

2.5.2 Fiber Chromatic Dispersion

Chromatic dispersion arises due to the dispersive property of the fiber, which causes different wavelength components to propagate at different velocities. This type of dispersion may be a concern if an optical carrier coexists with a lower and an upper sideband especially at 1550 nm region when single mode fiber is employed. Chromatic dispersion will in effect change the phase of USB with respect to LSB and lead to destructive interference. When ultimately 180° phase difference occurs between the upper and lower sidebands, complete elimination of the microwave signal might happen at the photodetector. This phenomenon limits the transmission distance. The phase shift between the sidebands depends on various parameters such as the center wavelength, fiber length and the modulating microwave frequency. Chromatic dispersion has been analyzed and reported in many papers and its effect is significant when the microwave signal is in the high mm-wave range [22], [20].

The RF power detected at the photodetector due to chromatic dispersion effects has a periodical fading and can be expressed as [23]

$$P_{RF} \propto cos^2(\frac{\pi L_f D \lambda^2 f^2}{c}) \tag{2.42}$$

where L_f is the fiber span, f is the RF carrier, λ is the optical carrier wavelength and c is the speed of light. D is the fiber dispersion parameter given by,

$$D = \frac{s_o}{4}(\lambda - \frac{\lambda_o^4}{\lambda^3}) \tag{2.43}$$

Here, s_o defines the zero dispersion slope and holds 0.087 $ps/nm^2.km$ and the zero dispersion wavelength λ_o is 1310 nm. D is typically 16.5 ($\sim$ 17) ps/(nm.km) for $\lambda = 1550$ nm single mode fiber. The argument of the cosine function in (2.42) implies that for a given radio frequency, the nulls will occur at the lengths that satisfy

$$L_{null} = \frac{kc}{2D\lambda^2 f^2} \qquad \text{for k } = 1, 3, 5... \tag{2.44}$$

In the topology given in Figure 1.1, the multiplexed microwave signals at the transmitter are sent over the fiber and then demultiplexed prior to detection at respective RAPs. The optical signal transmitted over the fiber consists of subcarriers, which have double sidebands. Figure 2.7 is plotted using equation (2.42) considering 1550 nm center wavelength. From this figure, the maximum length the WLAN signal at 2.4 GHz can travel is 660 km before chromatic dispersion eliminates the RF signal. 900 MHz signal even allows longer fiber span between the transmitter and the detector. The sideband cancellation occurs at 4700 km for 900 MHz. Hence, both RF signals can be transmitted over long distances and fiber chromatic dispersion is not a concern in this case. As the figure also indicates, the system's tolerance to chromatic dispersion induced fading decreases with the increase in the microwave frequency.

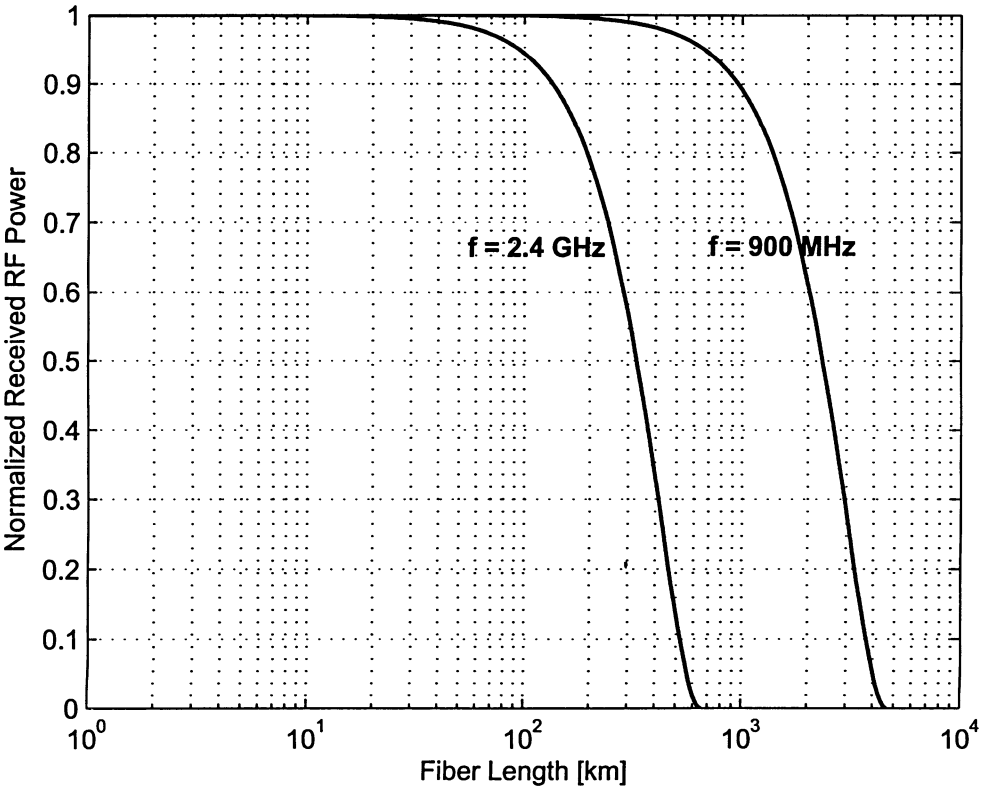

Figure 2.7: The effect of chromatic dispersion on the received RF power with the fiber length for RF signals at 900 MHz and 2.4 GHz.

Chapter 3

FBG Fabrication and Experimental Results

3.1 Fabrication of the FP-Based FBG

The Fabry-Perot (FP) based FBG employed in the experiments of this thesis was fabricated by applying the well established phase mask technology. The photoimprinting apparatus of this method is shown in Figure 3.1. KrF excimer laser emitted light at 248 nm with an energy of 348 mJ. The laser pulses were generated at a rate of 25 Hz with each pulse having a duration of 5 ns. This beam is radiated at normal incidence through an apodization (amplitude) mask, which consists of both the structure of a sinc function and the complementary sinc function. This mask is special in the sense that it is a double sinc apodization mask, which can induce two FBGs in the fiber. Non-apodized finite-length uniform fiber Bragg grating demonstrates a spectral response with undesirable sidelobes accompanying the main reflection peak. The sidelobes can be suppressed by designing gratings with a varying grating coupling coefficient along its length. This is called apodization, which is realized by photoinducing a refractive index grating with modulation amplitude that has a sinc function. Apodization mask eliminates the unwanted sidelobes other than the Bragg wavelength.

The apodized light next faced the phase mask, which is a flat slab of silica glass that is transparent to ultraviolet light. The phase mask is a periodical corrugated structure represented by a square profile. The role of the phase mask is to split the incident light

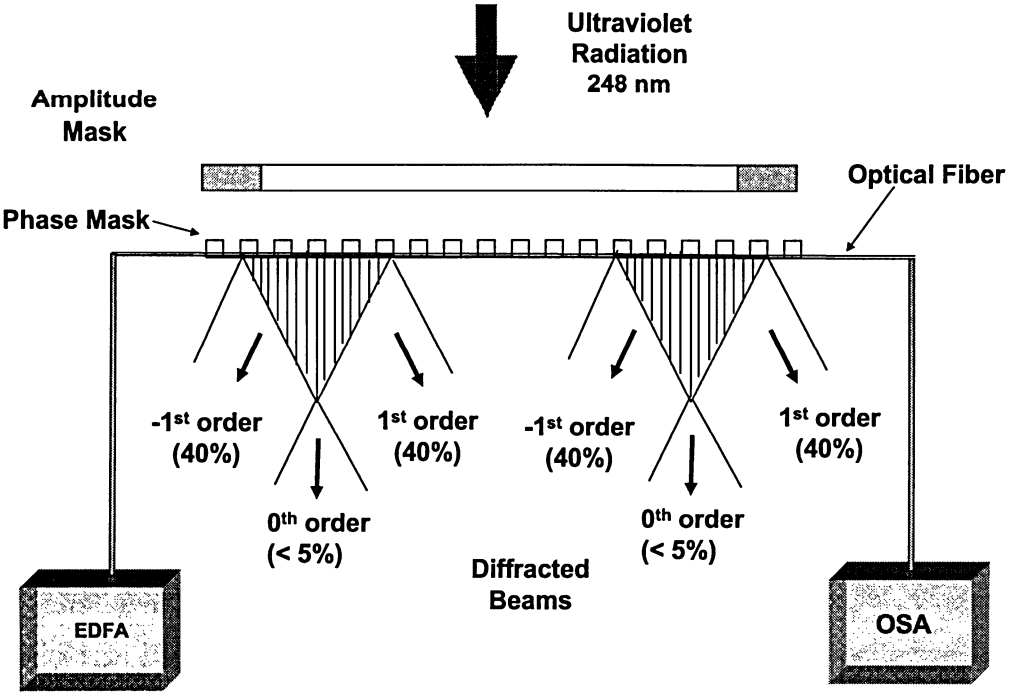

Figure 3.1: The setup used in fabricating fiber Bragg grating using Phase Mask technique

into diffraction orders. The mask confines light in the 0^{th}, $\pm 1^{st}$ and $\pm 2^{nd}$ orders. It is preferred not to have any incident light to reside in the zeroth order so that only -1^{st} and $+1^{st}$ orders are able to produce an interference (fringe) pattern in the core. The suppression of the light intensity in the zeroth order can be accomplished by adjusting the depth of the phase mask period accordingly when designing the mask [24]. In the course of writing the grating, 3% of the incident light was contained in the zeroth order while the -1^{st} and $+1^{st}$ orders each shared the same intensity of approximately 40%. It is important to note that the Bragg wavelength is independent of the UV source. Instead, the corrugation depth of the phase mask is selected in accordance with the UV wavelength. The period of the

photoinduced pattern in the core is primarily dependent on the phase mask period with the relation $\Lambda = \Lambda_{mask}/2$.

The protecting coat of the single mode fiber, preloded with hydrogen, was removed and then placed in close contact with the phase mask. The distance between the mask and the fiber is critical and has great influence in determining the level of photoinduced index modulation and thus reflectivity of the fabricated FBG. If the fiber is placed in contact with the mask corrugations, there is a possible damage to the corrugations of the grating. If the fiber is further away, such that the distance between the two interfering beams is much higher than the spatial coherence of the incident UV light, interference pattern fails to be produced. As a result, the grating cannot be formed. To achieve the maximum modulation in the refractive index, it can be said that the fiber should be placed away from the phase mask so that another fiber can be placed in between. Hydrogen loaded fiber was utilized to increase the photosensitivity, which allows the grating to be imprinted in the fiber. It is reported by [24] that with hydrogen loading, as high as 10^{-2} refractive index change can be achieved.

The grating was written in two stages. First, the apodization mask with two sinc functioned configuration was exposed to UV light. Then, the complementary of the mask was placed. The second step was carried out especially to smoothen the shape of the grating spectral response. The progress of the photo-inscription was followed by monitoring the grating's spectral profile on the spectrum analyzer with the erbium doped amplifier ASE (amplified spontaneous emission) as the source. The FBG was then annealed at a temperature of 150 $^{\circ}C$ for 15 hours to relieve the FBG from any residual unreacted hydrogen molecules and to prolong the lifetime of the grating.

Phase Mask technique has gained significant attention and it is particularly chosen due to its many benefits. Compared to other existing grating imprinting methods such as internal writing or holographic technique, phase mask method offers considerably higher performance. An ultraviolet excimer laser with relaxed coherency requirement can be used as the light source. Moreover, large volume of Bragg grating filters can be photo-imprinted simul-

taneously by a single exposure. This is enabled by positioning the fibers to be written in parallel to each other. In addition, this technique allows apodization to be performed; therefore, control over the spectral response of the Bragg grating is eased. Although the phase mask technique lends itself easily for mass production, a mask has the ability to write only a single wavelength or wavelengths in a small window. To fabricate gratings with individual wavelengths, different masks must be utilized.

3.2 Features of the Filter

The fabricated filter has two FBGs of 12 mm long separated by 4 mm. Figure 3.2 shows an illustration of the FP-FBG with an overall length of 28 mm. The center-to-center distance of the two FBGs was 16 mm that gave the spacing of adjacent resonance wavelength of $\sim$73 pm. The stop bandwidth of the FBG was $\sim$0.3 nm at -3 dB so five resonant peaks can be observed as shown in Figure 3.3. A broadband light source was used to obtain the FBG transmission. Note that in Figure 3.3, the resonant peaks were not fully resolved due to the limited resolution (15 pm) of the optical spectrum analyzer (OSA, Ando Corp. Model, AQ6317). Apparently, in order to measure an optic filter with a bandwidth at sub-pm level, a spectral resolution of several MHz is required. For example, 1 pm is $\approx$125 MHz in 1550 nm region ($\Delta f = c|\Delta\lambda|/\lambda^2$).

Since the microwave generator, used to modulate the optical carrier in this experiment, can step-scan the microwave frequency at 1 MHz resolution, one of the sidebands of the subcarrier was used to scan through the middle resonant peak as depicted in Figure 3.3. The experimental setup used to achieve this is shown in Figure 3.4. The laser was tuned to a wavelength that is 20 pm below the central resonant peak of the filter, 1536.5396 nm. The RF signal generator was scanned within 2 GHz frequency range with a step of 4 MHz. The Mach-Zehnder Modulator (MZM, JDS Uniphase OC-192 Modulator, 10024180) bias voltage was tuned so that the sidebands were visible. Otherwise, the OSA could not resolve the peak. Polarization controllers were situated before and after the MZM. The first one was used to match the polarization state of the laser with that of the MZM and the latter was

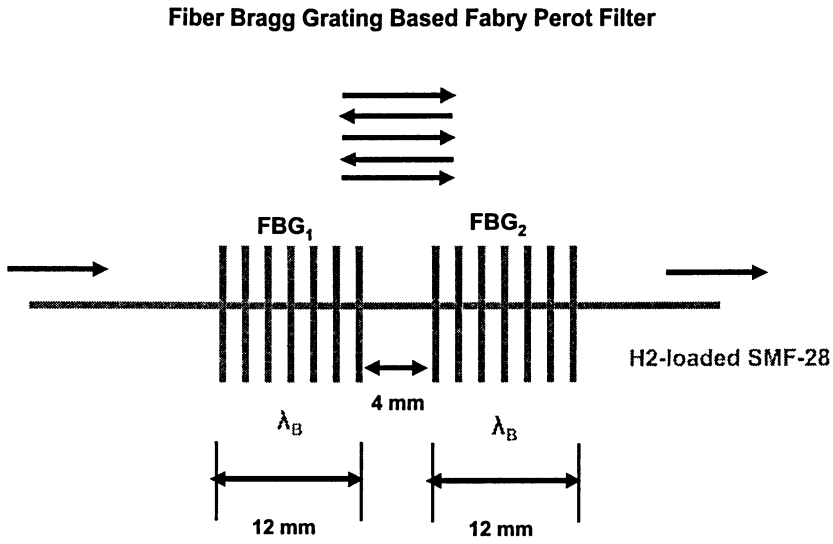

Figure 3.2: The fiber Bragg grating based Fabry-Perot filter

used to align the MZM output polarization with the filter. Polarization controller is an all-fiber based device that alters and controls the state-of-polarization (SOP) of light in the fiber by inducing stress, which causes birefringence. Birefringence refers to the difference in the refraction index of the fiber for plane polarized light vibrating parallel to the longitudinal axis of the fiber and the refractive index of the light vibrating perpendicular to the longitudinal axis. FiberPro polarization controller, for example, used in the experimental setup, has 3 paddles that act as waveplates. Each petal has groves, which allow the fiber to be looped around. Number of turns in each plate is dependent on the wavelength of operation. By adjusting the position angle of the paddles, the SOP is adjusted accordingly.

With the SOPs optimized, the resonant peak with a very narrow bandwidth was confirmed. This is shown by the upper solid trace in Figure 3.5. The filter has a bandwidth of

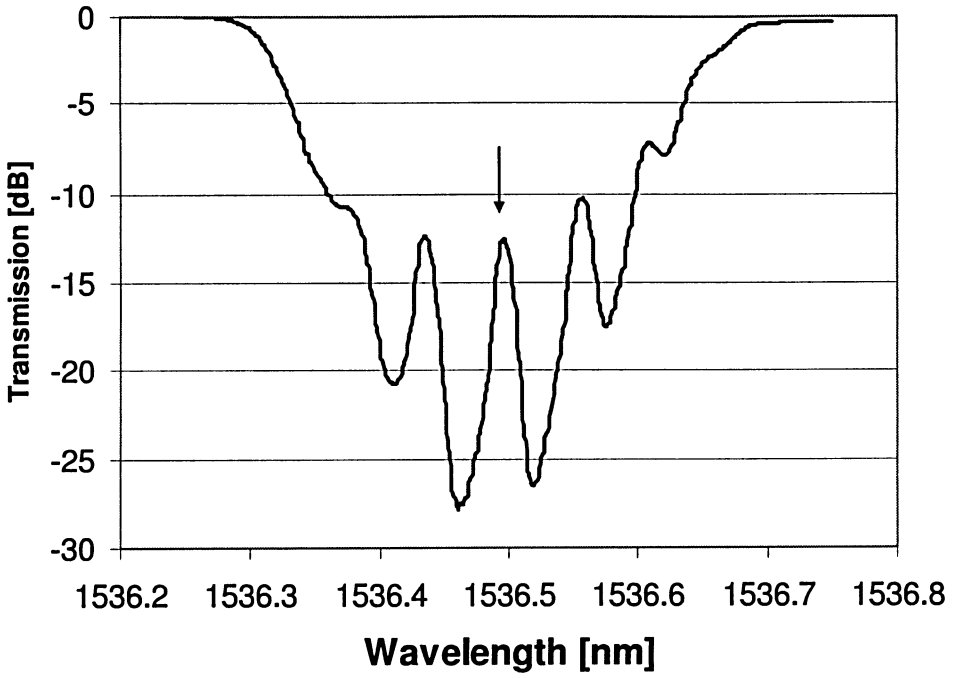

Figure 3.3: Transmission spectrum of the designed narrow bandpass filter. The spectrum was measured with an OSA at 15 pm resolution

120 MHz at -3 dB, 360 MHz at -10 dB and 1.5 GHz at -20 dB, respectively. The low insertion loss of about 0.8 dB at the central resonant peak was also confirmed. The FBG-based FP filter is an all-fiber device that can be relatively easily packaged with a thermally compensated design. The filter is so narrow that the effect of birefringence, caused by the laser radiation during fabrication, was observed as the splitting of the resonance peak depending on the polarization of the light source.

The polarization controller before the FBG was intentionally not aligned with the orientation of the laser output to see the significance of polarization. Figure 3.6 shows the scanned central resonant peak when the RF generator was set to sweep the peak within 0.5 GHz (4 pm) range. In the case of non-optimized SOP, the central resonant peak transforms into two peaks when compared to the trace obtained with adjusted SOP. It is evident that

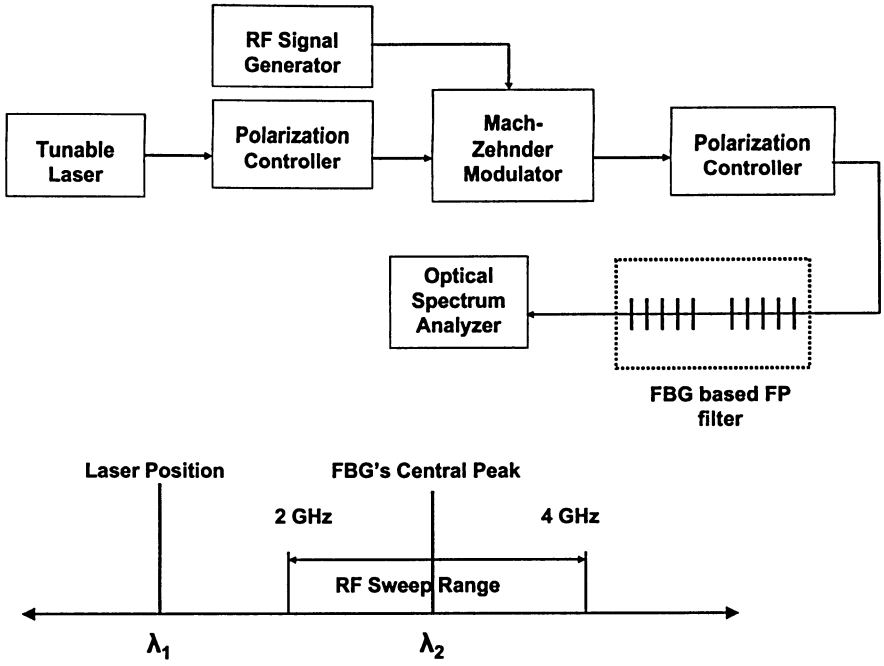

Figure 3.4: The block diagram of the setup used in sweeping the spectrum of the central resonant peak

the spectral bandwidth of the filter is broadened. For example, -10 dB bandwidth of the filter is increased from 360 MHz to 460 MHz. The peak of the filter suffers a loss of 1.7 dB. This degradation could be even higher at other poor polarization settings. Figure 3.6 indicates that the bandpass filter is a polarization sensitive device.

3.2.1 Comparison of the Fabricated Filter with a Planer FP

Numerical analysis on FP-FBGs prove that they have relatively close relation to planar FPs, which are constructed with two mirrors serving as the reflecting media [25]. The difference is that in FP-FBG, the phase or time delay is a function of wavelength and is dictated by the multiple reflections formed by the two gratings. The similarity between these types of FPs warrants the transmission response of the FP-FBG to be approximated by the theoretical

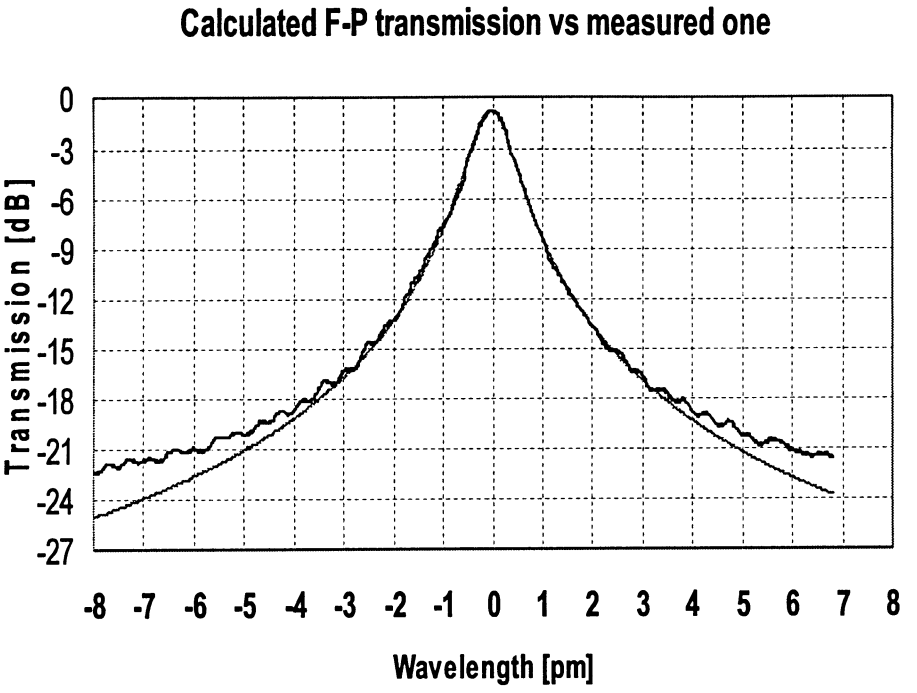

Figure 3.5: The spectrum of resonant peak (solid line), obtained by scanning the sideband over a 2 GHz range at 4 MHz per step. The thin line was the calculated resonant spectrum from a planer FP resonator

planar FP spectrum. In fact, fitting the experimental curve with the theoretical spectrum using FP analogy is the most straightforward approach as opposed to matrix or the boundary methods. The transfer function of the FP resonator cavity with respect to λ is given by [26]

$$T_{FP}(\lambda) = \frac{1}{1 + (\frac{2F}{\pi})^2 sin^2(\frac{\pi c}{n\lambda FSR})} \tag{3.1}$$

here, FSR is referred to as the free spectral range, the interval between the two respective transmission peaks and it is represented by,

$$FSR = \frac{c}{2nL} \tag{3.2}$$

where n is the refractive index of the medium of interest, c is the speed of light in free space

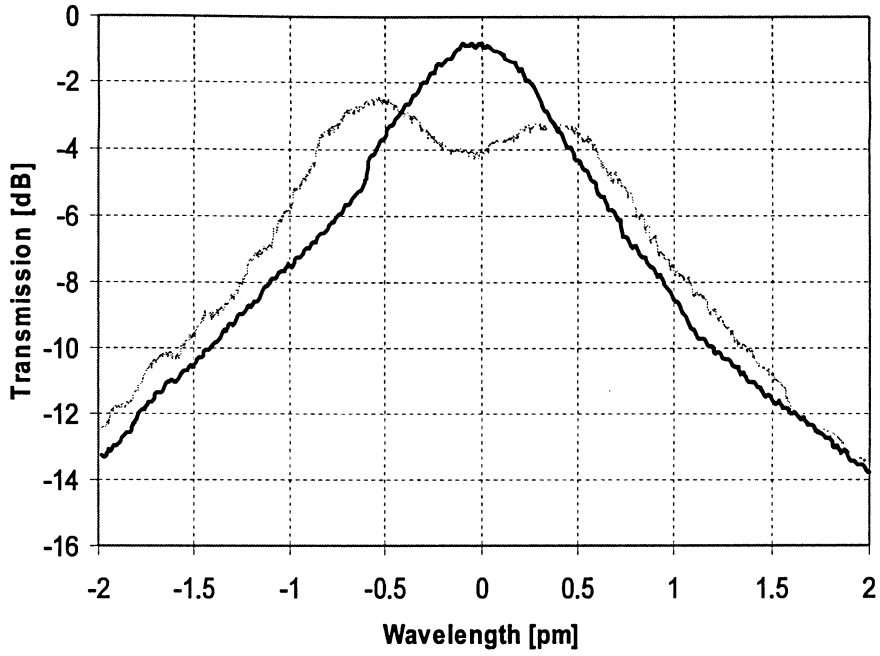

Figure 3.6: The central resonant peak scanned with the polarization state in non-optimal position. Faded trace is the non-optimized SOP case and the bolded trace represents the optimized SOP

and L is the distance between the two mirrors. In the calculation, L was substituted with the center-to-center spatial separation between the two FBGs (L=16 mm). F in the FP equation (3.1) is known as the finesse of the resonator and is described by the following:

$$F = \frac{\pi\sqrt{R}}{(1-R)} \tag{3.3}$$

R is the resonator reflectivity. The finesse of the fabricated filter is 76.95 and the free spectral range is ~73 pm (=9.125 GHz).

The spectral response obtained by scanning the central resonant peak of the filter is compared with the theoretical spectrum calculated from the planer FP resonator equation. As shown in Figure 3.5, the spectral profile fits reasonably well with a planer FP resonator

spectrum down to -15 dB if the resonator reflectivity, R = 0.96 was used. The reason for mismatch of the spectral tails is a subject of further study. One reason could be that the residual of amplified spontaneous emission from the laser had leaked into the photodetector. Similar results were obtained when the experimental spectrum was compared to the model based on the matrix method.

3.3 Experimental Setup

In order to achieve demultiplexing of subcarrier multiplexed cellular and WLAN signals at 900 MHz and 2.4 GHz respectively and to characterize the demultiplexer, number of experiments were performed. In the following sections, the performance and the feasibility of the designed sub-picometer filter together with an optical circulator in extracting 900 MHz from SCM signal was studied.

The block diagram of the experimental setup, analogous to a downlink in a SCM architecture, is shown in Figure 3.7. A microwave signal carrying 5 Mbps pseudorandom binary sequence in Binary Phase Shift Keying (BPSK) format at 900 MHz was generated by Vector Signal Generator (SMIQ 03B) by Rohde & Schwarz. Synthesized Signal Generator (HP-8673B) emulated another microwave signal at 2.4 GHz. These two RF signals were mixed via an RF power combiner. The optical modulation of the SCM radio signals was realized using the Mach-Zehnder intensity modulator, which was biased at a DC voltage corresponding to MZM's linear region of operation. The MZM has an insertion loss of 4.6 dB and supports a bandwidth up to 13.9 GHz. Since the MZM is polarization sensitive, a polarization controller (HP-11896A) was employed between the tunable laser and MZM to maximize the modulator output power. As a result of intensity modulation, at the MZM output, an optical signal consisting of the carrier and the corresponding upper and lower sidebands of the microwave signals was generated. 900 MHz and 2.4 GHz signals were offset from the carrier by ± 7.2 and ± 19.2 pm respectively. Figure 3.8(a) shows the MZM output when the DC bias voltage of the modulator was set at a non-linear region. Note that due to limited resolution bandwidth (of 15 pm) of the optical spectrum analyzer (OSA), only the

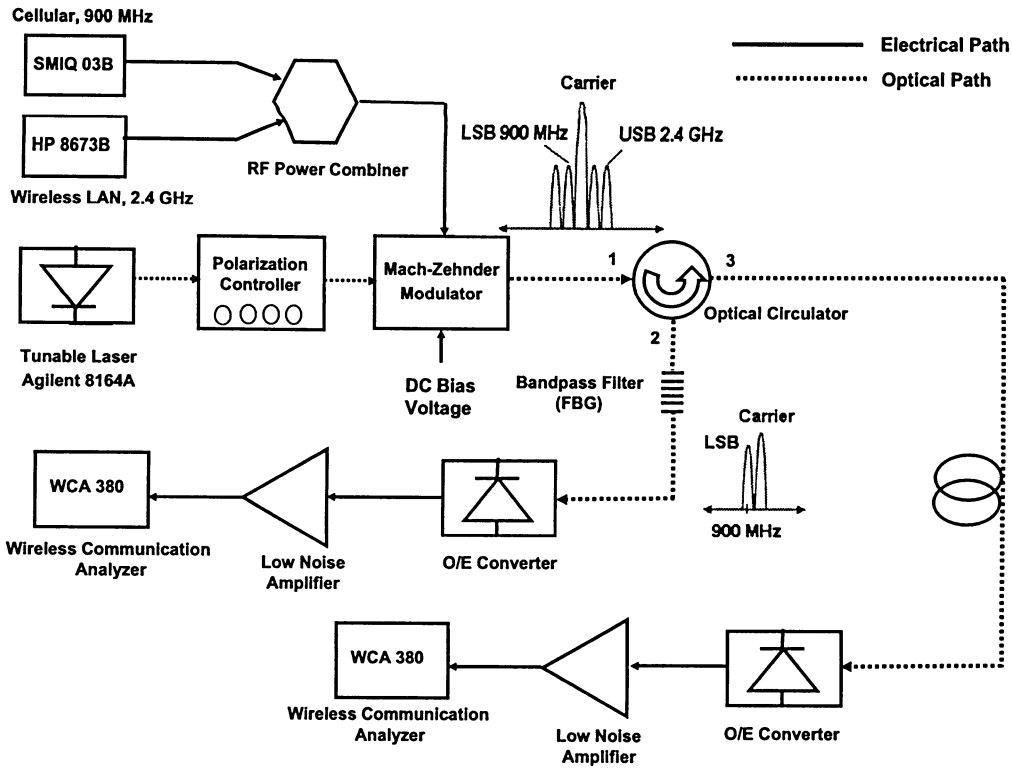

Figure 3.7: Experimental setup used for achieving demultiplexing of two subcarrier multiplexed microwave channels at 900 MHz and 2.4 GHz with the sub-picometer bandpass filter

respective sidebands of the 2.4 GHz could be partially distinguished from the carrier. As the modulating subcarrier frequency is decreased to 900 MHz, the sidebands appear to be embedded within the carrier spectrum; hence not visible. Figure 3.8(b) represents the MZM output under the same condition when the DC bias was tuned to linear region of operation. Still both sidebands of the subcarriers are there, but not quite visible.

The optical carrier along with the four sidebands as given in Figure 3.8(b) were fed into port 1 of the optical circulator. Optical circulator, a non-reciprocal passive device, plays the role of directing light from port-to-port sequentially in one direction starting from port 1 to 2. At port 2, a second polarization controller was placed before the filter. Following the

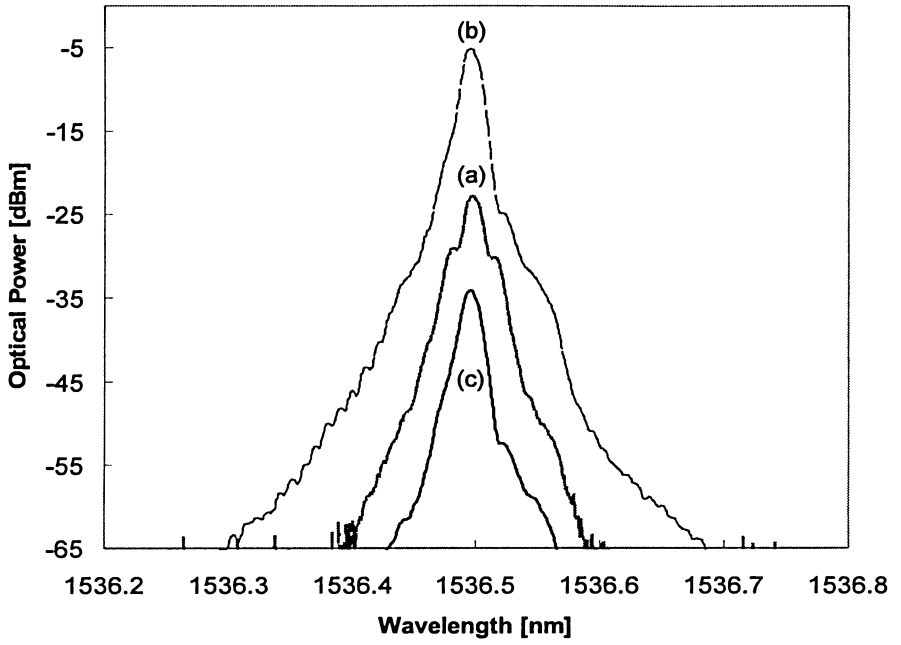

Figure 3.8: Optical spectra obtained on the optical spectrum analyzer. (a) output of the MZM when the DC bias was tuned to non-linear region (b) output of the MZM when the DC bias is tuned to linear region (c) lower sideband of the cellular signal selected by the filter

controller, the fabricated FBG in transmission mode was positioned to coincide the FBG's central peak (λ=1536.5396 nm shown in Figure 3.3) with the lower sideband of 900 MHz. Figure 3.8(c) shows the extracted lower sideband of the 900 MHz with partial optical carrier. The filter suppressed the carrier by ~22 dB while reflecting the non-matching channels including WLAN signal to port 3. Note that the carrier should not be completely removed to avoid clipping distortion in the RF signal [27]. At the filter output a carrier-to-sideband ratio (CSR) of ~3 dB was attained. CSR is the ratio of the peak carrier power to the peak sideband power of the selected channel. The CSR (with modulating signal) after filtering could not be measured directly due to the resolution constraint of the optical spectrum analyzer. The analyzer could not resolve the 2.4 GHz sideband (19.2 pm) from the 900 MHz

sideband (7.2 pm). Therefore, the CSR was obtained by measuring the optical powers of the carrier with and without microwave modulation. First, the optical carrier power of the modulated signal $P_T(mW)$ was measured after the filter with the RF signal on. Then, with the RF signal off, the optical carrier power $P_C(mW)$ at the filter output was measured. The CSR of the filtered signal was calculated with $CSR[dB] = 10log[P_C/(P_T - P_C)]$, which we defined.

The transmitted cellular signal was coupled to a high-speed, low distortion InGaAs PIN photodiode (OI-2125 O/E) by Tektronix. Following that, a low noise amplifier (LNA-ZX60-3011) by Mini-Circuits amplified the strength of the 900 MHz signal by ~15 dB to obtain sufficient power level as this is typically done prior to transmission over the hostile wireless channel in practical systems. Since the low noise amplifier (LNA) supports subcarriers from 400 to 3000 MHz, the residual WLAN signal after filtering is also amplified along with the cellular signal. Wireless Communication Analyzer (WCA 380) by Tektronix demodulated the microwave signal and recovered the data streams as well as record eye diagrams of the detected signal. Bit-error-rate, which was a key parameter in quantifying the signal quality, was estimated from the eye diagrams [28].

3.3.1 Bit Error Rate (BER) Estimation

The quality of the transmission of a digital signal is mostly judged by bit-error-rate (BER) performance. Measuring the bit-error-rate of a signal requires BERT, a BER tester, which can quantitatively show the ratio of bits received in error. However, BERT is costly and does not provide the reasoning behind why the errors have occurred. Therefore, eye diagrams or eye patterns as an alternative tool can be used in assessing quickly the reliability of the transmission medium and the transmission degradations. Eye diagrams are constructed by overlapping of random sequences of bits ones and zeros in terms of voltage. Rise times, overshoot, jitter and the degree of eye opening are few of the important parameters that can be measured and are useful in studying the noise or intersymbol interference in the signal.

When measuring the BER with practical instruments is not possible, estimating the BER

from eye diagrams is a viable solution. This is generally done by measuring Q-factor from the eye diagram. Several methods of determining Q-factor have been proposed in the literature.

Q-factor is analogous to electronic signal-to-noise ratio (SNR) if it is measured using a receiver and is defined by the following

$$Q = \frac{|\mu_1 - \mu_0|}{\sigma_1 + \sigma_0} \tag{3.4}$$

where, μ_i and σ_i are the mean and standard deviations of the ones and zeros respectively.

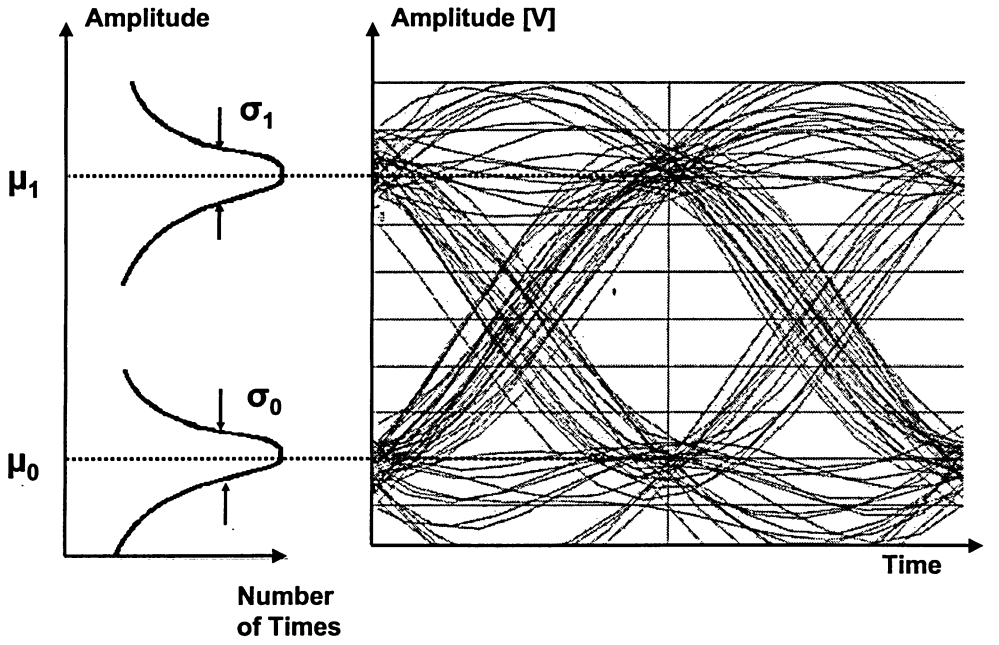

Figure 3.9: The eye diagram displayed on the Communication Analyzer and the representation of the parameters involved in calculating the Q-factor

Q-factor has a close relation with BER, which is expressed as [28]

$$BER = \frac{1}{2} erfc(\frac{Q}{\sqrt{2}}) \approx \frac{1}{(Q\sqrt{2\pi})} e^{\frac{-(Q^2)}{2}} \tag{3.5}$$

The approximation given in (3.5) is derived using the asymptotic expansion of $erfc(Q/\sqrt{2})$ and is reasonably accurate for $Q > 3$. The erfc is the complementary error function and is defined as

$$erfc(x) = \frac{2}{\sqrt{\pi}} \int_x^{\infty} e^{(-y^2)} dy \tag{3.6}$$

We developed a BER estimation algorithm written in Matlab. In the experiments, the eye diagram at the Wireless Communication Analyzer were post processed with this algorithm. Figure 3.9 shows an example of an eye diagram displayed on the WCA. In the algorithm, each recorded eye diagram on the WCA in bitmap image file are initially parsed. Images are then cropped to save processing time since only a small percentage of the eye diagram is needed. In the cropped region, the histogram traces for bits 1 and 0 in the eye diagram are recorded. From this data, the Q-factor and the BER are determined. To obtain reasonable sigma values (σ_1, σ_0), larger samples were taken, therefore larger window in the eye diagram. The larger width that is used, the larger the standard deviation and thus the larger the BER. This should be calibrated so that more realistic BER values are obtained.

This estimation method permits the eye diagrams to be tested regardless of bit rate, frame period or even modulation format. Since the Wireless Communication Analyzer has a sampling frequency higher than the signal data rate, more samples were acquired to minimize the estimation errors.

3.4 Experimental Results

3.4.1 Linearity of the Filter

Subcarrier multiplexed systems are known to suffer from nonlinear distortions. Nonlinear distortions include intermodulation and in-band distortions such as AM-AM and AM-PM.

Intermodulation distortion is a major concern with Cable TV systems while in band distortions are concerns with radio-over-fiber systems [1]. In fact, much research efforts have been put into linearizing electro-optical components to avoid nonlinearity. Therefore, the optical filter employed in the ROF link must demonstrate linear characteristics within the useful dynamic range. Dynamic range refers to the range of input RF powers over which the output power is above the noise floor and distortion-free.

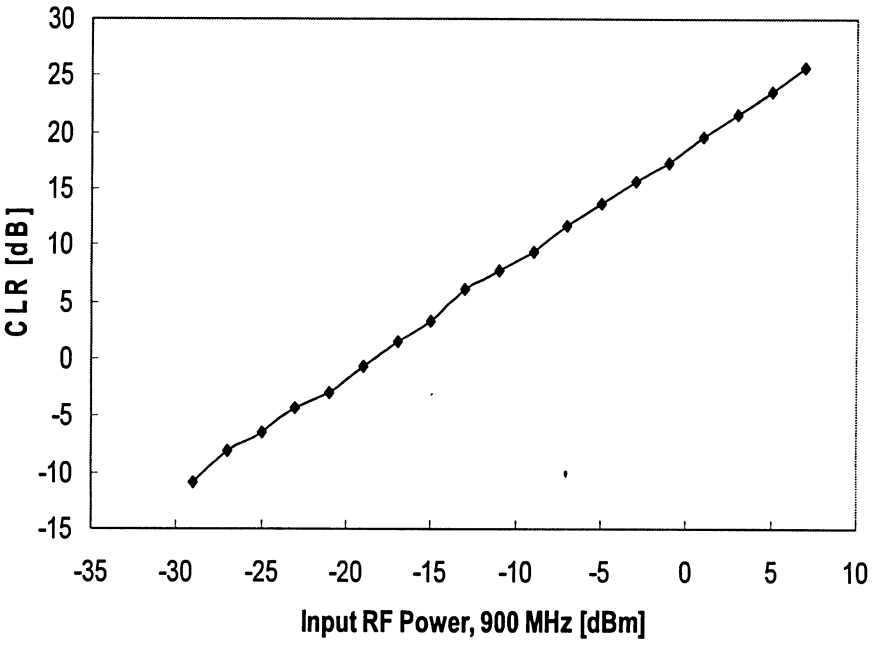

Figure 3.10: Carrier-to-leakage ratio (CLR) versus the input RF power of 900 MHz when the filter selected the 900 MHz signal and reflected the 2.4 GHz signal to circulator output port

In this section, linearity of the filter and the dynamic range supported by the proposed system were investigated. The SCM cellular and WLAN signals were applied to the MZM with equal RF power levels. The filter selected the 900 MHz signal while reflecting the 2.4 GHz signal. In this context, 2.4 GHz signal should not appear at the filter output; however,

a small amount of 2.4 GHz signal appears because of the filter leakage. Hence, carrier-to-leakage ratio (CLR) is defined as the ratio between the RF power at 900 MHz and the RF power at 2.4 GHz at the output of the filter. Figure 3.10 shows the CLR versus the input RF power at 900 MHz measured at the WCA. The WLAN signal's power remained constant. The figure suggests that the filter is almost linear from the input power of -29 dBm to 6 dBm.

Dynamic range is an important factor that needs to be addressed in the radio-over-fiber link. To assess the dynamic range of the system, the input RF power was varied from -38 dBm to +6 dBm. Figure 3.11 shows the relatively linear relation between the input and the output. This indicates that the bandpass filter had close to linear characteristics within a dynamic range of 44 dB. The dynamic range could be even higher, but this could not be verified due to the nonlinearity of the MZM. The RF power output from the signal generator could not be increased since increasing the RF power forces the modulator to behave in a non-linear manner.

3.4.2 Selectivity of the Filter

One of the challenging tasks in isolating two close optically modulated subcarriers is to have a filter with an adequate bandwidth and free spectral range. There must be compatibility between the available filter bandwidth and that of the RF channel. The filter should be able to pass the desired sideband while rejecting other channels.

In order to evaluate the selectivity of the demultiplexer, both the 900 MHz and the 2.4 GHz were applied simultaneously to the modulator with matching RF powers. Then, the input power of both signals were varied and the peak RF power levels at the output of the filter were measured by using the WCA. In this scenario, both signals were tones. Figure 3.12 shows that the filter had the ability to select the cellular signal with $\sim$25.5 dB discrimination compared to the WLAN signal. This selectivity was constant with the increase in input RF power. Note that despite the multiple resonant peaks existing in the stop band of the filter, only the middle peak was utilized. The other peaks are conveniently distant from the central

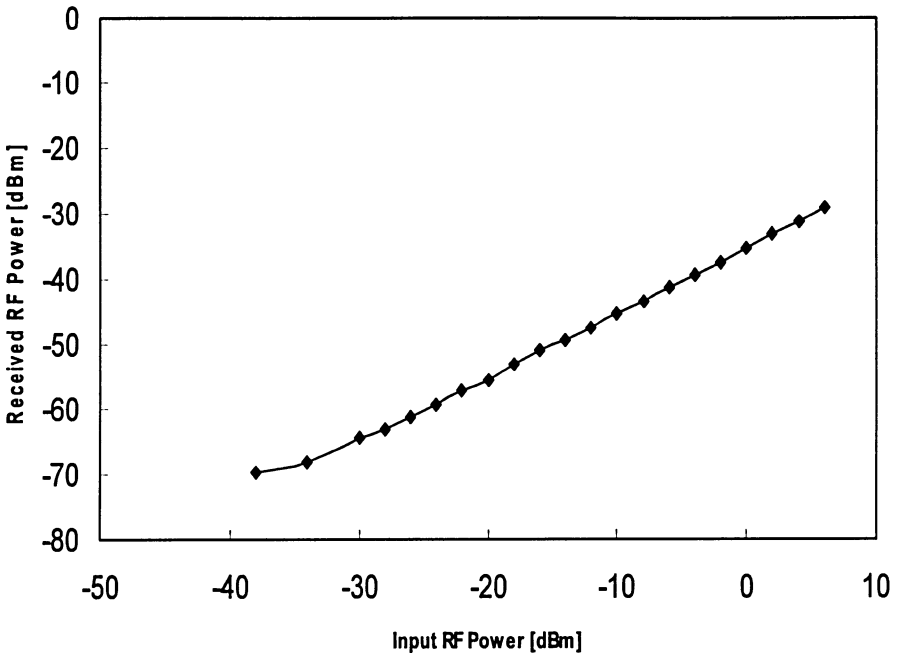

Figure 3.11: Received RF power versus input RF power of 900 MHz signal measured at the WCA when the 900 MHz signal is selected by the filter while the WLAN signal is reflected

peak; therefore, they do not play any role in the selection of the other cellular signal sideband or the WLAN signal sidebands.

Although the filter managed to suppress a substantial portion of the WLAN signal, some residual power, which we defined as leakage power, was observed. It was verified experimentally that this leakage had negligible impact on the cellular signal since an isolation of ~25.5 dB existed. Figure 3.13 displays the dependency of the leakage power on the input RF power of 2.4 GHz.

3.4.3 Frequency Separation of the Filter

The minimum allowed frequency separation between two subcarriers is determined by the bandwidth of the optical filter and the data rate of each subcarrier. The two subcarriers must

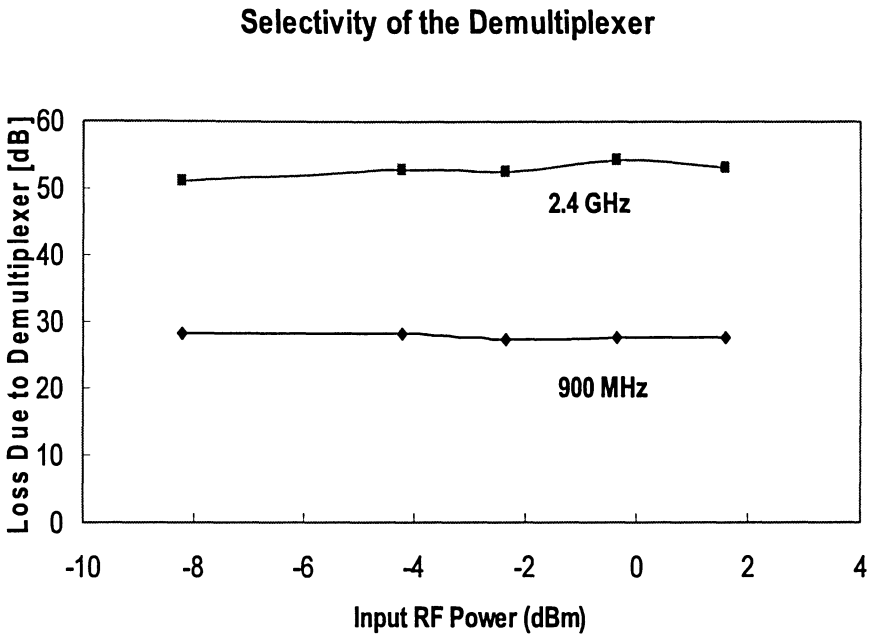

Figure 3.12: The degree of isolation that can be achieved by the filter

be distant enough to minimize the distortion and crosstalk imposed by the other subcarrier.

In order to determine the threshold frequency separation of the two subcarriers, the BER performance of 900 MHz signal at the filter output was measured as the 2^{nd} subcarrier was swept from 450 MHz to 1.1 GHz at the signal generator. The input RF power was +6 dBm and the 2^{nd} subcarrier had relatively identical power. Figure 3.14 demonstrates that the two subcarriers can be as close as 50 MHz before a significant increment of the BER occurs. The BER level at 50 MHz separation is $2.72 \text{x} 10^{-6}$.

3.4.4 Distortion Due to the Filter

The filter should not contribute to additional distortion to the transmitted and the reflected signals. In order to quantify the impact of FBG distortion, we compared the calculated BER

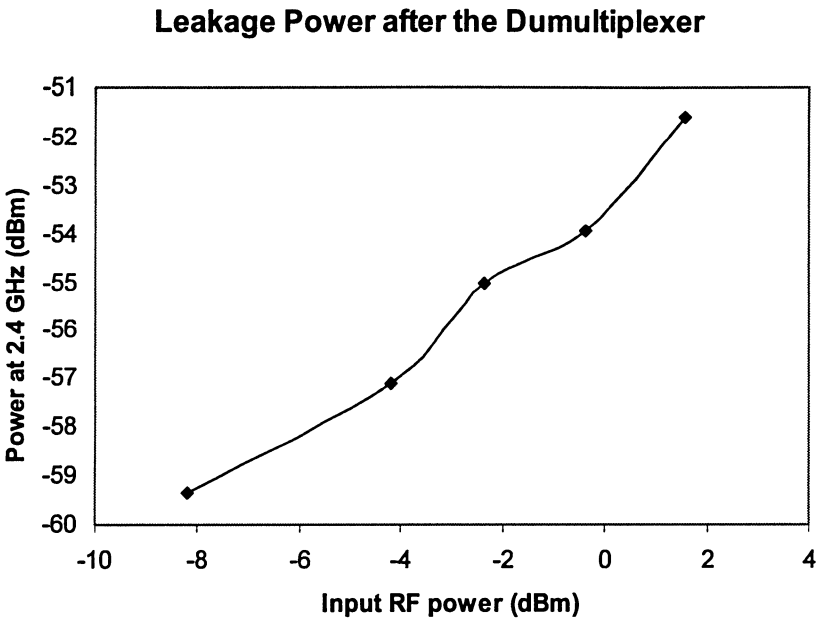

Figure 3.13: Leakage power in 2.4 GHz after demultiplexing versus the input RF power of 2.4 GHz at the filter output

of the selected signal (900 MHz) by the filter with the BER in the absence of filter. Figure 3.15 shows the BER of the cellular signal against the received RF power. The received RF power levels for the two scenarios were controlled by attenuating the received optical power. Almost identical BER response is seen between the filter input and output given that the RF power is same. This implies that despite going through the filter, the cellular signal maintains its BER level and therefore, the filter does not impose additional distortion.

The filter's performance was also evaluated using the eye diagrams of both the transmitted and the reflected signals. The cellular and the WLAN signals, applied to the power combiner, carried equal RF power. Figure 3.16(a) shows the corresponding eye diagram of the cellular signal at 900 MHz, which was transmitted by the filter. This figure demonstrates a very clear

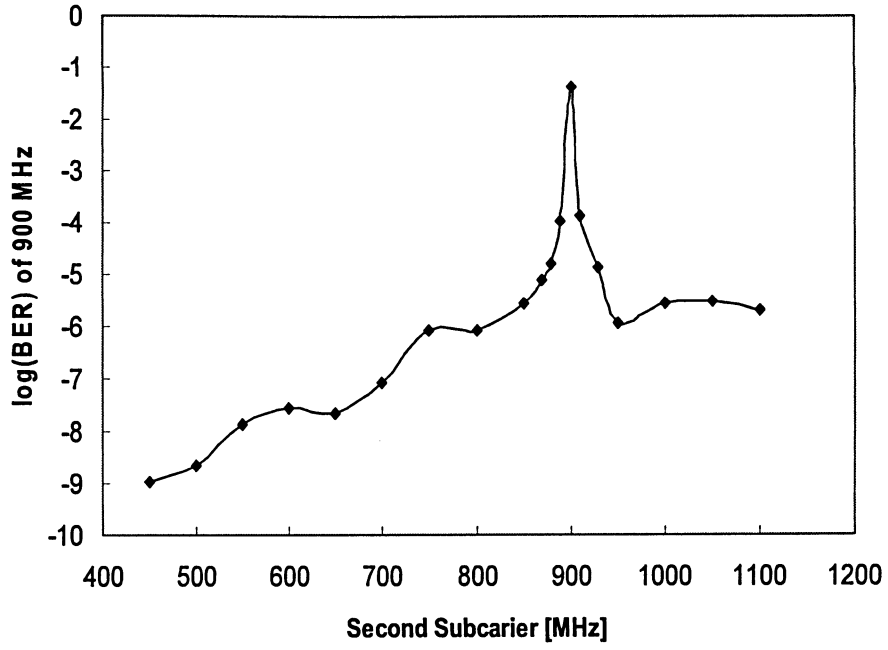

Figure 3.14: BER performance of 900 MHz when the 2nd subcarrier is scanned from 450 MHz to 1.1 GHz. This figure shows the minimum frequency separation of about 50 MHz permitted by the filter between two subcarriers

signal with a Q-factor of 7.201. Similarly, to examine the integrity of the reflected WLAN signal, 2.4 GHz at port 3 of the circulator was amplified subsequent to O/E conversion and then sent to WCA to be demodulated. Figure 3.16(b) represents the eye diagram of the WLAN signal at the circulator output. We also observe a very clear signal, which indicates that the filter does not significantly distort the filtered out signal. The reflected optical power was attenuated to obtain relatively same received RF power of ~ -30 dBm as the transmitted signal. The reflected signal has slightly worse eye diagram than the transmitted signal due to the attenuation. The Q-factor of this signal is 5.785.

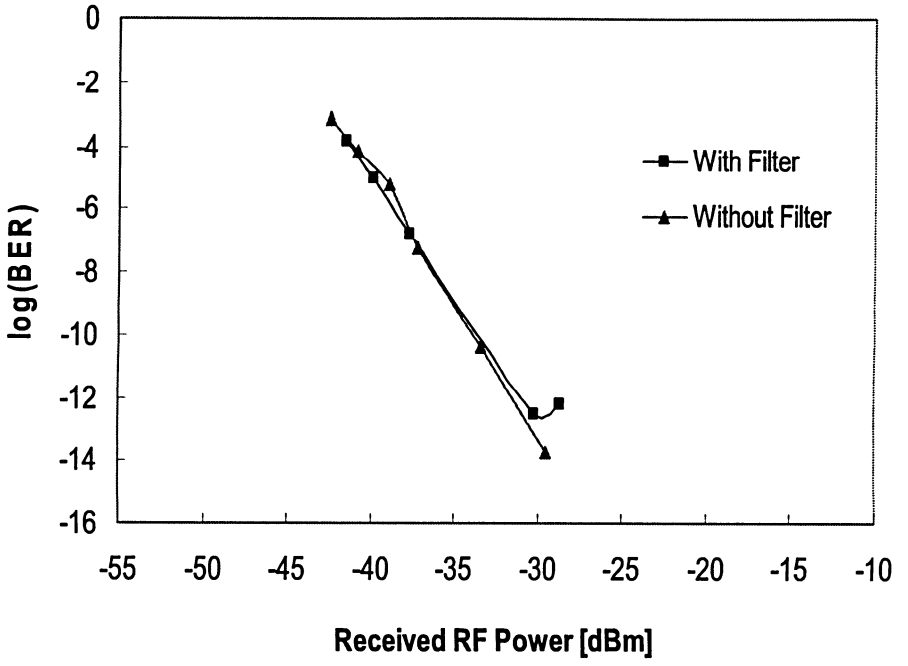

Figure 3.15: BER of cellular signal (900 MHz) versus the received RF power with and without filter

3.4.5 Beat Noise

When SCM optical signals are incident on the square-law photodetector, there could be beat noise due to mixing of the subcarriers. As shown in the analysis presented in section 2.4.1, the beating of the cellular USB in the reflected optical field with the WLAN signal and the carrier generates components. The properties of the noise depends on the number of subcarriers, the data rate, modulation format and frequency of the subcarrier. This type of noise is unavoidable particularly when the strong beating signals fall within the SCM bandwidth and contribute to additional noise. The accumulated noise degrades the system signal-to-noise ratio.

In our implementation, the residual upper sideband of the 900 MHz is reflected to port

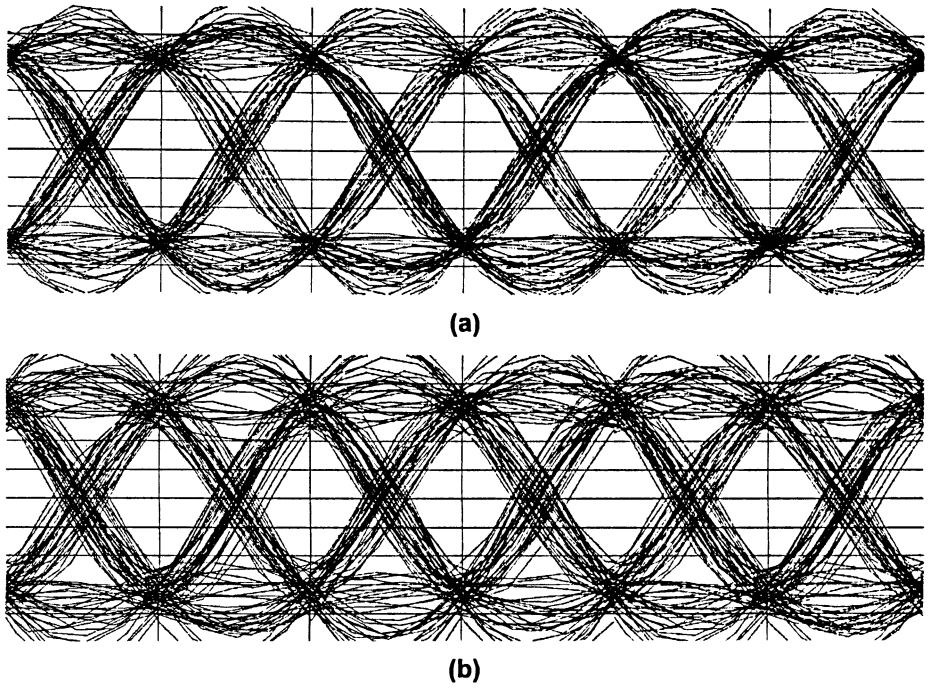

Figure 3.16: a) represents the eye diagram of the 900 MHz (selected) signal obtained at the output of the bandpass filter (b) is the 2.4 GHz signal (reflected) obtained at the output of the circulator (port 3)

3. The beating of this signal with the carrier and other sidebands upon detection by the photodetector may degrade the performance of the recovered 2.4 GHz subcarrier. To study this, we measured the BER performance of 2.4 GHz with the reflected RF power in the 900 MHz. Figure 3.17 shows the BER of 2.4 GHz when the RF ratio between the 2.4 GHz and 900 MHz was varied. The input RF power of 900 MHz was increased accordingly. We see that the beat noise is not a factor in our system since there is no significant variation in the BER level.

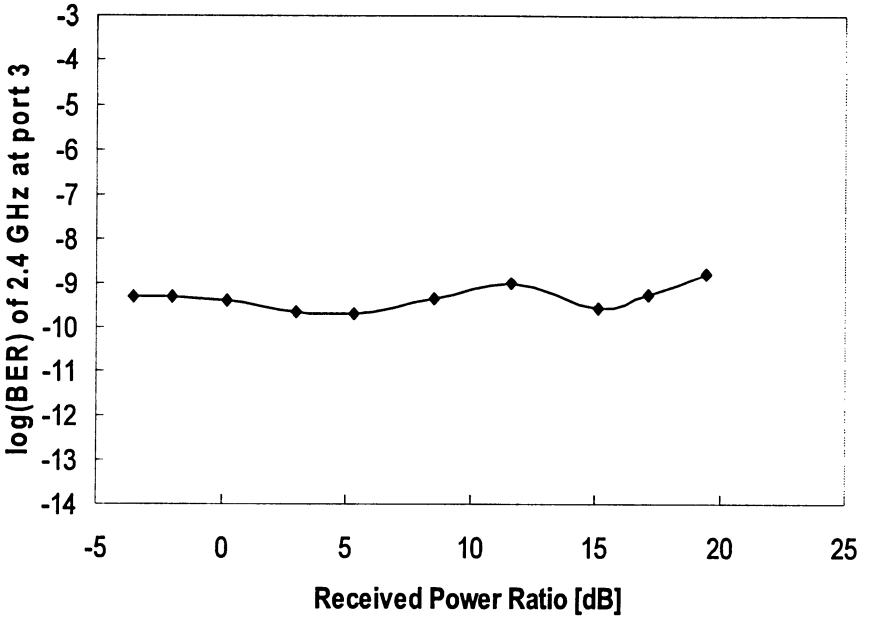

Figure 3.17: The BER performance of 2.4 GHz at port 3 with the power ratio of 2.4 GHz and 900 MHz

3.5 Carrier Suppression

In radio-over-fiber systems, the high level of unmodulated optical carrier power compared to the sidebands is an issue that needs close attention. The performance of the ROF link depends on the modulation depth. The modulation depth is limited by the nonlinear distortion of the optical modulator. In return, the dynamic range of the system will be considerably limited in strongly modulated systems. Therefore, the microwave signal is usually modulated weakly compared to the carrier to minimize the intermodulation effects as this was done in the analysis in section 2.4.1 and in the experiments. However, weak modulation will result in excess optical carrier power that will only reflect as useless direct current (DC) at the receiver. This DC component may force the photodetector to saturate and can even

cause damage. In addition, DC current at the detector translates to shot noise and hence decreases the signal-to-noise ratio (SNR) of the link. Therefore, particularly in remote applications, the optical carrier, which bears no information, must be reduced to achieve a high modulation depth and consequently enhance the sensitivity of the detector.

Number of techniques has been proposed to maintain a high modulation depth and FBGs have been found to perform exceptionally well [29]. This was confirmed also by us in Gu et al. [30], where a single subcarrier was considered. In this section, the aim was to quantify the transmission efficiency improvement when two subcarriers were mixed. Figure 3.18 shows the BER of 900 MHz signal with and without filtering with respect to the received optical power. The received optical power was adjusted using an optical attenuator. Two observations can be deduced from this figure. At the same received power of -32 dBm, the 900 MHz signal with the filter can achieve a BER of 10^{-12}, which is significantly better than the 10^{-3} BER with the unfiltered signal. This could be because in the unfiltered case, the optical signal has subcarrier sidebands of the WLAN and the cellular signals as well as the strong optical carrier carrying no information. In comparison, the cellular lower sideband together with the suppressed carrier are confined in the filtered signal. To achieve a BER of 10^{-9} with the filter, the received power is at -34.59 dBm; however, without the filter the received power should be higher at -27.61 dBm. An improvement of $\sim$7 dB was experienced in the receiver sensitivity. This improvement in the sensitivity is carrier-to-sideband ratio dependent. As the CSR level is reduced, the sensitivity increases non-linearly. In this experiment, the CSR was $\sim$3 dB. With the same filter, not only extracting the cellular signal from RF modulated optical signal was possible but the carrier power was also considerably suppressed which in return increased the modulation depth.

3.6 Cellular Upper Sideband Suppression

The optical signal at port 3 of the circulator still encompasses the upper sideband of the cellular signal. To isolate this signal completely from the WLAN sidebands, a second filter is required. However, the filter should have a resonant peak that can be matched dynami-

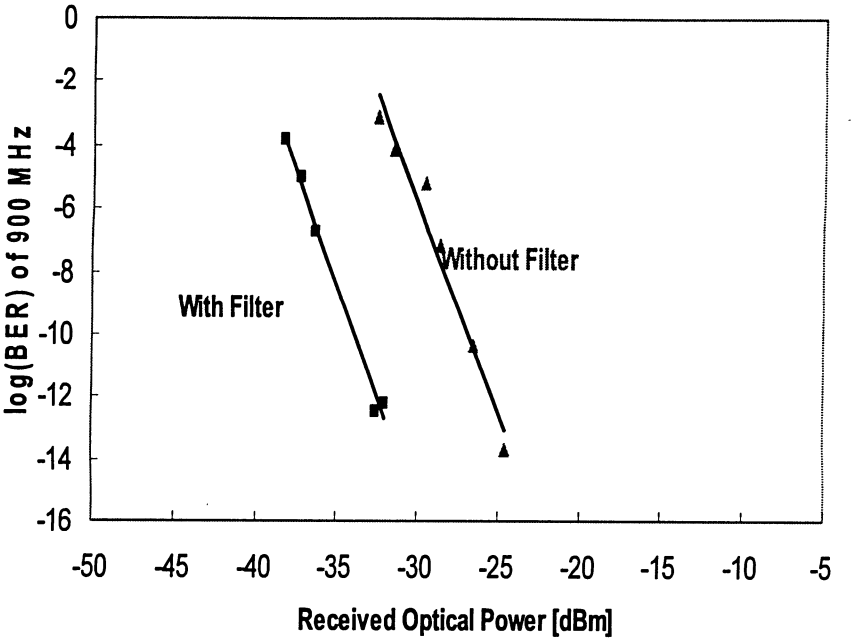

Figure 3.18: BER versus the received optical power of 900 MHz with and without filtering.

cally/adaptively to the upper sideband. This issue can be tackled by using a tunable optical filter.

We incorporated a second FP-FBG at the circulator output. The fabrication of this filter was similar to the one discussed in the earlier sections. Transmission response of this filter is shown in Figure 3.19. The filter has broader stop band and the bandwidth of the central resonant peak is wider. This peak on a larger scale is shown in Figure 3.20. The -3 dB bandwidth of the filter is 6 pm = 750 MHz and the -6 dB bandwidth is 10.4 pm = 1.3 GHz. The insertion loss at the central peak is only 0.175 dB. The grating was observed to be insensitive to the variation in the polarization state. In addition, as it is also evident in Figure 3.20, a discrimination of 15.2 dB is provided by the middle peak.

This uniform FBG is not tunable in nature; however, the Bragg wavelength can be varied

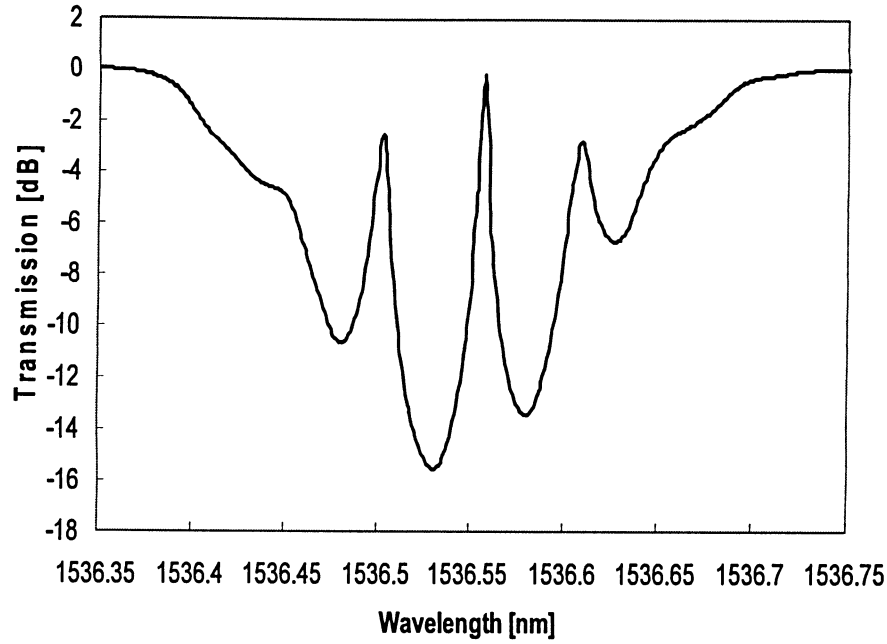

Figure 3.19: The transmission spectrum of a second Fabry-Perot based fiber Bragg grating

by stretching the length of the FBG. FBG has great elastic properties. Bragg wavelength depends on the core effective index of refraction and the grating periodicity and these parameters are subject to change with tension, which consequently shifts the Bragg wavelength. Stress induced change in the Bragg wavelength is given by [31]

$$\Delta\lambda_{Bragg} = 2(\Lambda\frac{\partial n}{\partial L_g} + n\frac{\partial \Lambda}{\partial L_g})\Delta L_g \tag{3.7}$$

where n is the index of the core. Equation (3.7) accounts for the change in the refractive index and the grating spacing. This expression can be given by

$$\Delta\lambda_{Bragg} = \lambda_{Bragg}(1 - p_e\epsilon_z) \tag{3.8}$$

where p_e is the effective strain-optic constant expressed by the following:

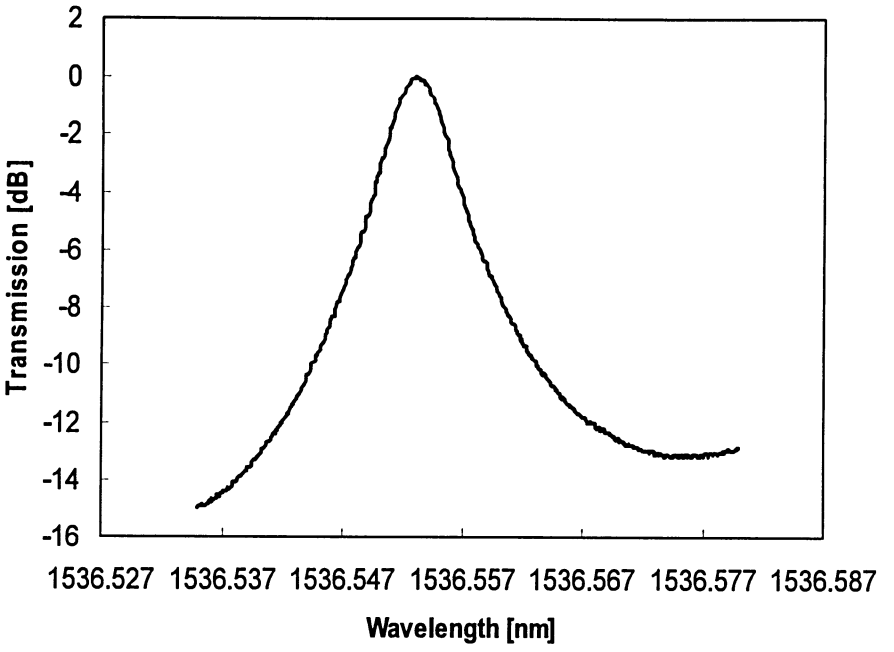

Figure 3.20: The central resonant peak of the filter shown with a larger scale

$$p_e = \frac{n^2}{2}[p_{12} - \nu(p_{11} + p_{12})] \tag{3.9}$$

where p_{11} and p_{12} denote the strain-optic tensor components, ν is the Poisson's ratio. $p_{11} = 0.113$, $p_{12} = 0.252$, n=1.482 and ν=0.16 are generally the values of a single mode fiber. Under these conditions, 1 $\mu\epsilon$ translates to 1.2 pm shift in the center wavelength of the grating at $\sim$ 1550 nm operation.

To provide strain in micro range, the FP-FBG was mounted on a structure between two flat plates. The magnitude of stretch in the grating length was achieved by adjusting the micrometer which in return varied the distance between the two plates.

The second FP-FBG was stretched to coincide with the upper sideband of the 900 MHz. Note that the LSB of 900 MHz was selected by the first FP-FBG. The WLAN signal at this

filter's output was at most 12 dB higher in strength than the cellular signal. However, this isolation was not stable.

Chapter 4

Discussions and Future Work

4.1 Discussions

To increase the robustness of the system following can be done:

- The wavelength of the laser can be locked. Since the laser wavelength was tuned to match the LSB of the cellular signal with the center peak of the first FBG that has a bandwidth in the sub-picometer range, any slight drift in the wavelength could cause variation in the received optical power.

- Due to environmental effects such as temperature, FBGs' peaks may shift slightly. It is well known that the Bragg wavelength shifts by 10 pm for every $1°C$ variation in the temperature. This requires the laser to be adjusted accordingly. Nevertheless, the variation in the wavelength is possible to overcome. Since the length of the FBG is 28 mm, it can be relatively easily packaged with a temperature-compensation design.

4.1.1 Chromatic Dispersion Issues

In our experiment, the length of fiber varies between 2 to 3 meters. However, our system is capable of allowing fiber length to be much longer as verified in section 2.5.2 since microwave signals are at sub-GHz range. Both signals can be jointly transmitted over ~600 km of fiber before chromatic dispersion affects the system severely. This implies that the optical demultiplexer can be installed within this span with the chromatic dispersion as the least

concern.

4.1.2 Power Loss and Noise in the Experimental Setup

The signal transmitted from port 1 to 2 incurred a power degradation of ~1.30 dB and from 2 to 3 is ~2.2 dB in the optical circulator. These include the loss in the pigtails used to connect the circulator with other devices. The MZM has an insertion loss of 4.6 dB. To establish connection between the devices, fiber connectors together with fuse splicing was used. Each connector and splice contributed a loss of ~1 dB and ~0.03 dB respectively. Signal attenuation in the fiber is negligible with 0.2 dB/km at the 1550 nm wavelength band due to short spans used in the proposed system. Misalignment in the fiber and dirt on the pigtail surface can lead to additional loss. The loss in the optical domain is twice as much when converted to electrical. The relative intensity noise parameter of the laser was -145 dB/Hz.

4.2 Conclusions

The primary goal of this thesis was to investigate optical demultiplexing of radio multimedia signals in a SCM FTTC architecture analytically and experimentally. Cellular wireless signal at 900 MHz and a WLAN signal at 2.4 GHz were jointly transmitted over an externally modulated ROF link. An optical signal processing method was studied in separating the cellular signal from the WLAN signal to exploit many benefits all-optical demultiplexing promises. To achieve this, we fabricated a novel sub-picometer fiber Bragg grating bandpass filter. This filter, fabricated by inducing resonance between two identical FBGs, has a -3 dB bandwidth of 120 MHz and a fairly low insertion loss of 0.8 dB. When the FP-FBG's transmission spectrum of the central resonant peak was fit with the numerically computed spectrum based on a classical FP equation, a good agreement was observed.

We experimentally verified that this filter could be applied as an optical bandpass filter in extracting subcarrier multiplexed 900 MHz cellular signal from 2.4 GHz WLAN signal optically. Experimental results showed that with this filter, an isolation of ~25.5 dB between

the cellular and WLAN signal could be achieved. Moreover, the filter has a linear response; it permits the channel separation to be as low as 50 MHz between two subcarriers and introduces negligible distortion to both the transmitted and the reflected signals. In the experiments, excess dc power resulting from externally modulating the optical carrier was reduced significantly. Thus, we eliminated the potential increase in the shot noise level by filtering out the carrier prior to detection. In return, we increased the modulation index.

The analysis in Chapter 2 revealed that owing to the relatively low frequencies of the microwave signals, the SCM system can tolerate chromatic dispersion. Furthermore, additional dispersion due to the filter was insignificant since low data rates were carried in the system. The experimental results showed that the fabricated filter is a promising candidate in demultiplexing multimedia radio signals at low GHz range in optical domain. It is evident that the appreciably narrow bandwidth of the filter allows demultiplexing of closely spaced subcarriers effectively. By using array of such filters that have low insertion loss and insignificant distortion, demultiplexing of more than two subcarriers is also possible.

4.3 Future Work

In the experiments, due to resource limitations, the BER was approximated by calculating the Q values from the post-processed eye diagrams. Obtaining the Q values with high precision is very crucial since the BER is solely dependent on the Q values. Although several eye diagram samples were processed, the result would still differ from the ideal case. The estimation can be avoided by implementing a test bed that employs BERT to measure BER more accurately.

It is difficult to completely demultiplex two densely distributed microwave signals optically partly because of the double sideband regime utilized in the experiment. We can suggest two approaches:

1. An optical FBG bandpass filter capable of isolating signals in one step can be designed. The filter should have spectral response such that the two cellular sidebands and the

partial carrier are selected together at port 2 whereas the WLAN signal will be reflected to port 3.

2. Single sideband modulation techniques can be applied to simplify filtering process. One can argue that an FBG with broader reflection bandwidth can be designed to filter out the upper sidebands of the two signals leaving the other sidebands to go through complete demultiplexing with a narrow filter. However, this approach is not efficient since the RF power is wasted. Instead single sideband (SSB) modulation can be adopted. The Mach-Zehnder modulator can be replaced by a dual-electrode Mach-Zehnder modulator which generates an SSB signal at the transmitter. Moreover, another method based on SSB modulation, where all the RF power is transformed into one sideband can also be considered as a possible solution.

Moreover, in this thesis, emphasis on the demultiplexing of subcarrier multiplexed cellular and WLAN signals in a downlink was given. In future, similar experimental investigation can be performed in an uplink arrangement. In the uplink scenario, the system will be more demanding since the signals first face the non-linear hostile wireless channel, which degrades the signal due to multipath fading, path loss and other factors. In addition, extensive mathematical analysis can be performed and the results obtained can then compared with the ones obtained from the experiments.

Bibliography

[1] R. Yuen and X. Fernando, "Analysis of sub-carrier multiplexed radio over fiber link for the simultaneous support of WLAN and WCDMA systems," *Kluwer Wireless Personal Communications Journal, Special Issue on Advances on Wireless LANs and PANs*, vol. 33, issue 1, pp. 1–20, 2005.

[2] A. Doufexi, E. Tameh, A. Nix, S. Armour, and A. Molina, "Hotspot wireless LANs to enhance the performance of 3G and beyond cellular networks," *Communications Magazine, IEEE*, vol. 41, pp. 58 – 65, 2003.

[3] A.P. Foord, P.A. Davies, and P.A. Greenhalgh, "Optical demultiplexing for subcarrier multiplexed systems," *IEEE Transactions on Microwave Theory and Techniques*, vol. 43, issue 9, pp. 2324 – 2329, September 1995.

[4] P.A. Greenhalgh, R.D. Abel, and P.A. Davies, "Optical prefiltering in subcarrier systems," *Electronics Letters*, vol. 28, issue 19, pp. 1850 – 1852, September 1992.

[5] J. Capmany, D. Pastor, A. Leon, P. Chamorrow, and D. Santos, "Experimental demonstration of optical prefiltering in WDM-SCM optical networks employing ultraselective optical bandpass filter," *Electronics Letters*, vol. 35, issue 4, pp. 318 – 319, February 1999.

[6] X. Fernando, H. Kosek, Y. He, and X. Gu, "Optical domain demultiplexing of subcarrier multiplexed cellular and wireless LAN radio signals," *Proceedings of the SPIE Conference Photonic North, Photonic Applications in Nonlinear Optics, Nanophotonics, and Microwave Photonics*, vol. 5971, pp. 59711S1–10, September 2005.

[7] H. Kosek, Y. He, X. Gu, and X. Fernando, "All-optical demultiplexing of closely spaced multimedia radio signals using sub-picometer fiber Bragg grating," *Under Review for* IEEE *Journal of Light Wave Technology*, Summer 2006.

[8] S. Weisser et al., "Dry-etched short-cavity ridge-waveguide MQW lasers suitable for monolithic integration with direct modulation bandwidth up to 33 GHz and low drive currents," *Proc. ECOC*, pp. 973 – 976, 1994.

[9] C. H. Cox III, E.I. Ackerman, G.E. Betts, and J.L. Prince, "Limits on the performance of RF-over-fiber links and their impact on device design," *IEEE Transactions on Microwave Theory and Techniques*, vol. 54, issue 2, pp. 906 – 920, February 2006.

[10] H. Al-Raweshidy and S. Komaki, *Radio Over Fiber Technologies for Mobile Communications Networks*, Norwood, MA: Artech House Publishers, 1^{st} Edition, Boston, MA, 2002.

[11] J. M. Senior, *Optical Fiber Communications:Principles and Practice*, Prentice Hall, 2^{nd} Edition, Boston, MA, 1992.

[12] X. Fernando and H. Kosek, "Improved expression for intensity noise in multimedia over fiber networks," *Under Review for IEEE Transactions on Broadcasting*, Winter 2006.

[13] G. Keiser, *Optical Fiber Communications*, McGraw-Hill, 3^{rd} Edition, Boston, MA, 2000.

[14] Optical Society of America, *Fiber Optics Handbook*, New York ; Toronto : McGraw-Hill, 2002.

[15] A. Othonos, "Fiber bragg gratings," *Review of Scientific Instruments*, vol. 68, issue 12, pp. 4309 – 4341, December 1997.

[16] C. Martinez and P. Ferdinand, "Analysis of phase-shifted fiber Bragg gratings written with phase plates," *Applied Optics*, vol. 38 issue 15, pp. 3223 – 3228, May 1999.

[17] S. Legoubin, M. Douay, P. Bernage, P. Niay, S. Boj, and E. Delevaque, "Free spectral range variations of grating-based Fabry-Perot filters photowritten in optical fibers," *JOSA A*, vol. 12, issue 8, pp. 1687 – 1694, August 1995.

[18] B.G. Korenev, *Bessel Functions and Their Applications*, Boca Raton, FL: CRC Press, 2002.

[19] B.J. Eggleton, G. Lenz, N. Litchinitser, D.B. Patterson, and R.E. Slusher, "Implications of fiber grating dispersion for WDM communication systems," *IEEE Photonics Technology Letters*, vol. 9, issue 10, pp. 1403 – 1405, October 1997.

[20] C. Marra, A. Nirmalathas, D. Novak, L. Reekie C. Lim, J.A. Besley, and N.J. Baker, "The impact of grating dispersion on transmission performance in a millimeter-wave fiber-radio system," *IEEE Photonics Technology Letters*, vol. 14, No. 9, pp. 1345 – 1347, September 2002.

[21] K. Kitayama, T. Kuri, K. Onohara, T. Kamisaka, and K. Murashima, "Dispersion effects of FBG filter and optical SSB filtering in DWDM millimeter-wave fiber-radio systems," *IEEE Photonics Technology Letters*, vol. 20, issue 8, pp. 1397– 1407, August 2002.

[22] U. Gliese, S. Norskov, and T.N. Nielsen, "Chromatic dispersion in fiber-optic microwave and millimeter-wave links," *IEEE Transactions on Microwave Theory and Techniques*, vol. 44, issue 10, part 1, pp. 1716 – 1724, October 1996.

[23] E. Vourch, D. Le Berre, and D. Herve, "A WDM fiber-radio experiment incorporating a wavelength-self-tunable single-side-band filter," *Microwave Symposium Digest, 2002 IEEE MTT-S International*, vol. 3, pp. 1703 – 1706, June 2002.

[24] K. O. Hill and G. Meltz, "Fiber bragg grating technology fundamentals and overview," *Journal of Lightwave Technology*, vol. 15, issue 8, pp. 1263 – 1276, August 1997.

[25] X. Peng and C. Roychoudhuri, "Design of high finesse, wideband Fabry-Perot filter based on chirped fiber Bragg grating by numerical method," *Opt. Eng.*, vol. 39, pp. 1858 – 1862, July 2000.

[26] B.E.A. Saleh and M.C. Teich, *Fundamentals of Photonics*, New York ; Toronto : Wiley, 1991.

[27] R. Hui, B. Zhu, R. Huang, C.T. Allen, K.R. Demarest, and D. Richards, "Subcarrier multiplexing for high-speed optical transmission," *Journal of Lightwave Technology*, vol. 20, issue 3, pp. 417 – 427, March 2002.

[28] P.C. Becker, N.A. Olsson, and J.R. Simpson, *Erbium-doped Fiber Amplifiers :Fundamentals and Technology*, Academic Press; San Diego, CA, 1999.

[29] M. Attygalle, C. Lim, G.J. Pendock, A. Nirmalathas, and G. Edvell, "Transmission improvement in fiber wireless links using fiber Bragg gratings," *Photonics Technology Letters, IEEE*, vol. 17, issue 1, pp. 190–192, January 2005.

[30] X. Gu, Y. He, H. Kosek, and X. Fernando, "Transmission efficiency improvement in microwave fiber-optic link using sub-picometer optic bandpass filter," *Proceedings of the SPIE Conference Photonic North, Photonic Applications in Nonlinear Optics, Nanophotonics, and Microwave Photonics*, vol. 5971, pp. 597123–1–6, September 2005.

[31] A. Othonos and K. Kalli, *Fiber Bragg Gratings: Fundamentals and Applications in Telecommunications and Sensing*, Norwood, MA, Artech House, 1999.